The Time Of Flight Spectrometer of the BGO-OD Experiment

Peter Meiß

Ich versichere, dass ich diese Arbeit selbstständig verfasst und keine anderen als die angegebenen Quellen und Hilfsmittel benutzt sowie die Zitate kenntlich gemacht habe.

Bonn, ...
                Datum   Unterschrift

1. Gutachter: Prof. Dr. Hartmut Schmieden
2. Gutachter: PD Dr. Wolfgang Hillert

Contents

iv

Introduction

The elementary particles known today are quarks, leptons and exchange bosons. The interaction between these particle types is described by the Standard Model. Matter surrounding us is composed of electrons, neutrons and protons. While the electrons belong to the class of leptons and are elementary, protons and neutrons have a common substructure of three valence quarks determining the measured properties, surrounded by a sea of quark-antiquark pairs contributing to the mass. Due to the common substructure, they are both referred to as nucleons. The force keeping quarks bound to the nucleon and binding the nucleons to each other in atomic nuclei is the strong interaction, which is transmitted by the gluon as exchange particle. The excitation spectrum of nucleons is predicted by the standard model. However, more resonances than actually found until today are predicted. Furthermore some of the experimentally verified resonances were found to have energies deviating severely from the predictions. Strong interaction is described by its coupling constant $\alpha_S(Q^2)$. For small distances between the interacting quarks, corresponding to a high momentum transfer from a probe particle, the coupling constant asymptotically approaches zero. At such distances, the interacting quarks are quasi-free particles, and perturbation theory is usable to describe the interaction theoretically. For large distances, corresponding to a small momentum transfer, the coupling constant rises to larger values. Perturbation theory cannot be used anymore, making an experimental investigation inevitable. Information about the strong interaction for small momentum transfers can be extracted by examining the excitation spectra of nucleon resonances, which decay mainly into mesons. By using photons as probe particles, the 4-momentum transfer becomes as small as possible. The BGO-OD[1] experiment at the ELSA[2] accelerator facility of the University of Bonn is specifically set up for such experiments. A photon beam of known energy is used to excite nucleon resonances, and the complete experimental setup is sensitive to detection of mixed final states. Identification of the charged particles in forward direction is realized with a magnetic spectrometer and time of flight measurement, making the time of flight detector an essential component of the complete experimental setup.

A time of flight detector using components of the former SAPHIR[3] experiment was characterized and set up and tested within the course of this thesis.

After a short overview of the components used within the BGO-OD experiment in chapter 2 and a discussion of the technical and physical properties of the time of flight detectors in chapter 3,

---

[1] *B*ismuth$_4$*G*ermanium$_3$*O*xide$_{12}$-*O*pen*D*ipole

[2] *EL*ektronen *S*tretcher *A*nlage; http://www-elsa.physik.uni-bonn.de/

[3] *S*pectrometer *A*rrangement for *P*hoton *i*nduced *R*eactions, http://saphir.physik.uni-bonn.de/

two different test procedures using cosmics and their results are discussed in chapter 4.

A Sampling - ADC and pulse shape analysis software is used for convenient setup of detector parameters and diagnosis of the time of flight detector. The pulse shape analysis software developed within this thesis and the used sampling-ADC hardware is discussed in chapter 5. First results of test measurements with the complete time of flight spectrometer within the BGO-OD experiment will be presented in chapter 6. followed by a conclusion and outlook in chapter 7.

The BGO-OD Experiment at ELSA

Before giving a detailed description of the time of flight spectrometer in the next chapter (3), a brief description of the components within BGO-OD experiment will be given here. The BGO-OD experiment is supplied with an electron beam of up to 3.5 GeV by ELSA. An overview of the accelerator is shown in fig. 2.1, with the BGO-OD experimental area in the upper left. A side view of the BGO-OD experiment is shown in fig. 2.2, with the electron beam comes from the left. At the BGO-OD experiment, *photon tagging* is used to convert the incident electron beam to a photon beam of known energy. Multiple bremsstrahlung radiators are available within a goniometer system. Copper radiators are used for creation of an unpolarized photon beam, and a diamond is available for creation of a polarized photon beam. After an incidetn electron has transmitted a part of its kinetic energy to a photon, the electron is deflected by a magnet and detected in the tagging system. The remaining energy of the electron before hitting one of the tagging detectors is calculated from the deflection angle in the magnetic field, and the energy of the bremsstrahlung photon is given by the difference to the beam energy provided by ELSA, e.g. the photon is *tagged*. The photon beam then impinges on a liquid hydrogen target within the *BGO* central detector, eventually producing excited states. The decay products in forward direction are then tracked by MOMO and SciFi2 before entering the *O*pen *D*ipole magnet. Behind the magnet, the decay products are tracked by a set of drift chambers, before eventually reaching the *T*ime *o*f *F*light detector, which will be discussed in detail in the next chapter (3). Using the tracking detectors before and after the magnet, full particle trajectories are calculated. Together with the timing information provided by the time of flight detector, identification of charged particles is possible. This procedure is explained in sec. 3.3.
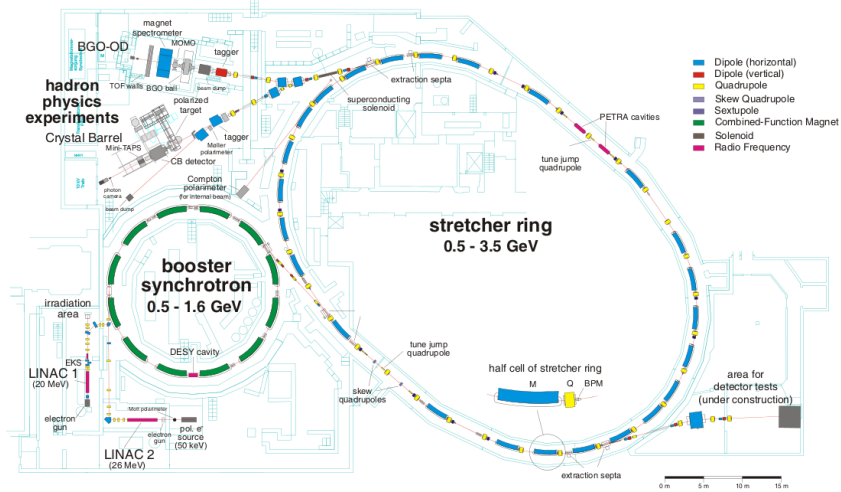
Figure 2.1: An overview of the ELSA accelerator facility. The BGO-OD experimental area is situated in the upper left.
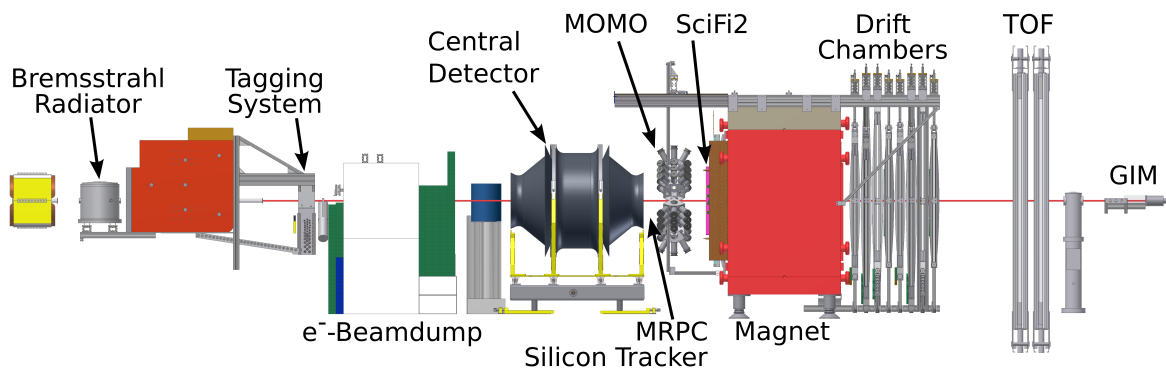
Figure 2.2: An overview of the BGO-OD experiment.

The Time Of Flight Spectrometer

The Time of Flight Spectrometer, short ToF, is used to detect charged and neutral particles and measure their flight times, as the name implies. With known traveled distance of the particles, their velocities are calculated. Together with known particle momentum, this information is used to identify charged particles. For detection of charged and neutral particles with a good time resolution, plastic scintillation detectors are ideally suited. After providing some technical details for the ToF spectrometer in the first section, plastic scintillation detectors will be discussed in some detail in the second section of this chapter. The chapter will conclude with a discussion of particle identification using the ToF spectrometer.

3.1 Technical Details

For the ToF spectrometer set up in the course of this thesis, a total of 22 plastic scintillation detectors of the SAPHIR experiment are used. Due to geometrical constraints of the SAPHIR experiment, scintillators of the dimensions $3400 \times 210 \times 60$ mm and $2700 \times 200 \times 45$ mm were used. A cutaway drawing of such a detector is shown in fig. 3.1. The scintillator material used is "NE110" of Nuclear Enterprises. These scintillator blocks are wrapped in a layer of reflective aluminium foil for light recollection. For mechanical stabilization, the scintillation material is supported by a block of "ROHACELL" with 32 mm thickness, sandwiched between two aluminium plates of 0.10 mm thickness. A layer of black tape is wrapped around the complete detector structure for protection against outside light and physical damage of the inner wrapping during handling of the detectors. Scintillation light is read out on both ends of the detector as shown in 3.2 by using fishtail lightguides with 210 mm and 200 mm length and attached Philips XP2020 photomultiplier tubes (short PMTs or PMs). Eight of the long detectors are arranged horizontally in a wall structure (fig. 3.4a). For convenience, naming of the previous ToF setup is reused, and this detector wall is called "ToF3". Detectors of this wall will be labeled *LongHorizontal* with an appended index. 14 short detectors are arranged vertically (figs 3.4b and 3.3). This arrangement is called "ToF4". Detectors of this wall will be labeled *ShortVertical*. Both detector walls have a gap for the photon beam of 200 mm in central position. The support structures of both walls were developed by O. Jahn [1]. Due to the hardware limitations of the current setup, the time resolution required for BGO-OD is not achieved. An extension of the ToF setup to provide sufficient time resolution is being set up at the moment, and will be discussed shortly in the following.
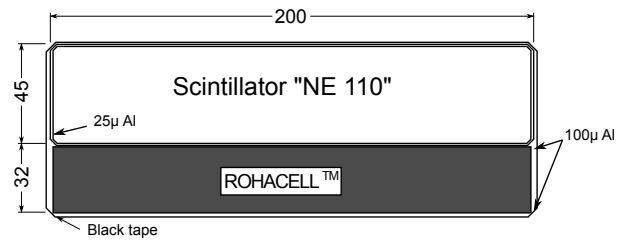
Figure 3.1: Cutaway drawing of a SAPHIR detector [2].
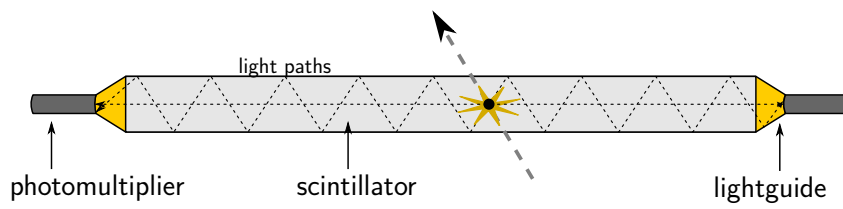
Figure 3.2: A ToF detector with possible light paths to the PMs
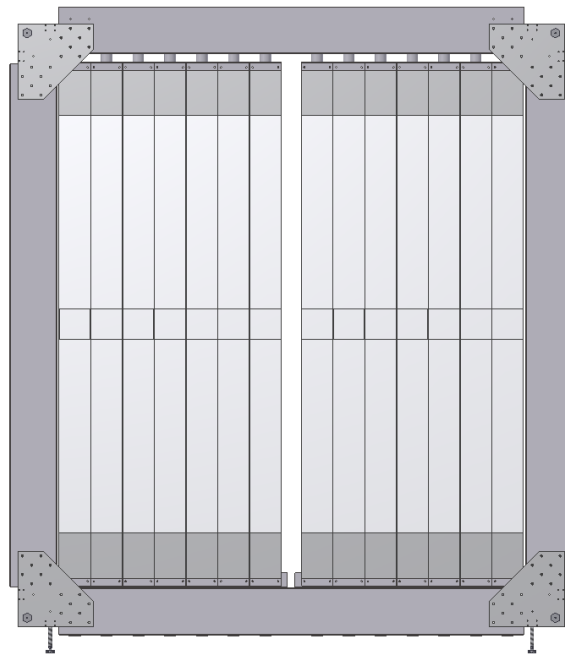
Figure 3.3: Outline of ToF4 [1]
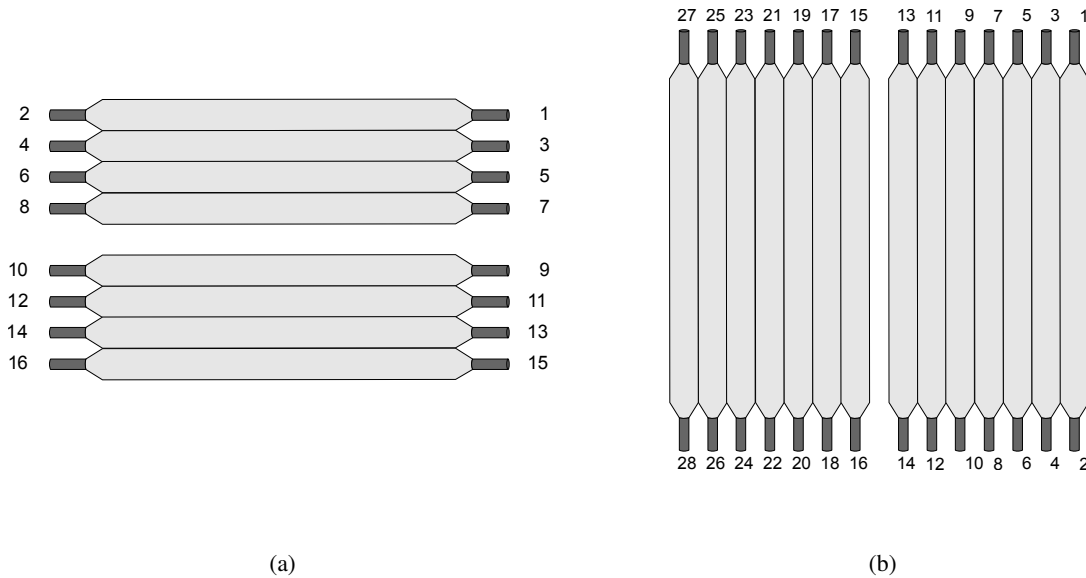
Figure 3.4: Outline of ToF3 (a) and ToF4 (b) with channel indices; looking in beam direction

3.2 Plastic Scintillation Detectors

For an exact measurement of flight times, a good time resolution of the detectors is inevitable. Due to the large size of the detectors, a sufficiently large attenuation length of the detector material is needed as well. Time resolution and attenuation length will be discussed in detail in secs. 3.2.7 and 3.2.4. Both properties are given by scintillators. They belong to the organic scintillators and are composed of a polymer as support material, doted with a fluorescent component and a wavelength shifter. Energy deposited in the scintillator material by crossing ionizing radiation is transformed in scintillation light by the fluorescent component. The wavelength shifter then absorbs the scintillation light, and re-emitts it at a wavelength where optimal transparency of the base polymer is given. This usually corresponds to wavelengths in the visible spectrum. If a sufficiently large detector is used, neutral particles can as well be detected by by ionization caused by recoil protons. Because plastic is used as supporting material, detectors of almost arbitrary size and shape can be realized. Depending on the used materials, plastic scintillation detectors reach attenuation lengths of up to a few meters, combined with signal rise times of down to below one ns. In the case of NE110, PVT [1] is used as support polymer, which is doted with Anthracene as fluorescent component and POPOP[2] as wavelength shifter. For NE110, signal rise times of around one ns and an attenuation length of around 4 m can be expected. It is ideally suited for use in the ToF detector, and was therefore chosen as scintillator material for the SAPHIR experiment [2]. Since the scintillator material is subject to degradation due to aging and radiation damage, the characteristic properties of the detectors have to be determined again before usage in the BGO-OD experiment.

---

[1] Polyvinyltuol

[2] a benzene compound, emission wavelength around 410 nm

3.2.1 Energy Deposition by Ionizing Radiation

Energy deposition by ionizing radiation in particle detectors is described in great detail in [3], [4] and [5]. The explanation given in this section is based roughly on the material of [5]. Charged particles traveling through matter interact with shell electrons, stripping them from their nuclei if enough energy is transferred during interaction. The energy region of interest for cosmics and the BGO-OD experiment lies between a few 100 MeV up to a few GeV. In this region, the mean energy loss dE of heavy[3] charged particles along an infinitesimal path length dX is described by the Bethe-Bloch equation.

As the particle travels along the detector and interacts with the shell electrons, during each interaction, an amount of energy δE can be transferred to the shell electron. To remove the shell electron from its nucleus, a minimum energy δE_{min} corresponding to the ionization potential is needed. The maximum energy transfer δE_{max} happens in case of a head on collision with the incident particle, and is limited by the kinetic energy of the incident particle. Between δE_{min} and δE_{max}, the probability to deposit a certain amount of energy is roughly given by $P(\delta E) \propto \frac{1}{\delta E^2}$ [5], leading to a sharp peak for the minimum energy δE_{min}, and an asymptotic drop towards zero until δE_{max} is reached. The total energy deposited in the detector material is then given by the sum over all interactions $\Delta E = \sum \delta E$, and each δE will follow the statistical distribution given by $P(\delta E)$. The probability of a certain amount of energy ΔE to be deposited in a "thin" detector is described by the Landau-distribution. Energies above δE_{min} contribute to the Gaussian-like distribution for the lower energies of the spectrum, while the tail of the Landau-distribution towards higher energies is caused by the asymptotically decreasing probability for head on collision with an energy transfer of δE_{max}. For increasing detector thickness, a longer distance to release small amounts of energy becomes available, whereas the probability for a head on collision releasing the total incident kinetic energy remains the same. This will lead to a broadened peak in the Landau distribution, and for sufficiently thick detectors, it approaches a Gaussian shape. The "thickness" of the detector, corresponding to the shape of Landau distribution, is mainly related to the ratio $K = \frac{\overline{\Delta E}}{\Delta E_{max}}$ of the mean energy loss $\overline{\Delta E}$ given by the Bethe-Bloch equation and the maximum possible energy transfer ΔE_{max}. This ratio can be calculated for different particles, energies, detector materials and sizes, as it was done by Landau, Vavilov and many others. For a cosmic myon, even a layer of 1 m of water can be considered as only moderately thick, while for heavy slow particles, e.g. protons below 1 GeV, even only 1 cm of water would be sufficient to produce a nearly Gaussian energy distribution. [5].

For the energy distributions encountered during the cosmic tests of the ToF detectors (sec. 4) therefore Landau distributions are expected. During later testing within the BGO-OD beam line (sec. 6), the shape of the energy distribution will depend on the amount of slow and heavy particles still able to reach the ToF detectors.

3.2.2 Light Propagation

Scintillation light emitted at an arbitrary position along the detector can reach a PM either by taking a direct path or by reflection along the detector walls (fig. 3.2). The possible paths for direct light depend on the solid angle visible by the photomultiplier, which is given by

$$\Omega = \frac{F}{X^2}$$

with the PM surface F and the distance X to the PM. Paths of reflected light are limited due to the critical angle of total reflection $\Theta_c(n) = \frac{1}{n}$ in the case of air surrounding the detector. If light hits the

---

[3] heavier than the electron, e.g. $m > m_e$

detector wall at a lower angle, it will leave the detector and cannot reach the PM. Θ_c therefore gives an upper limit to the path length of reflected light, as the longest possible path is given for angles slightly larger than Θ_c. Most of the reflected light will have such angles, and the path length of reflected light is approximated by the refraction index of the scintillator. For NE110, the manufacturer gives a value of $n = 1.6$ [6]. The measured speed and attenuation of light traveling along the detector are influenced by the different intensity contributions and path lengths, as will be discussed in the following sections 3.2.3 and 3.2.4.

3.2.3 Effective Speed of Light

For a common point of origin along the detector, the relation between direct and reflected distances traveled through the detector is given by

$$d_{\text{ref}} = n \cdot d_{\text{dir}} \ .$$

Reflected and direct light both propagate with the velocity of light in medium. Due to the longer distance traveled, the reflected component will take considerably more time to cross the distance to the PM. The *effective speed of light* is the velocity, at which the reflected light would have to travel on an assumed direct path to the PM. The relation to the velocity of light in medium of the direct light and the velocity of light in vacuum is given by the refraction index as

$$c_{\text{ref;eff}} = \frac{1}{n} c_{\text{dir;med}} = \frac{1}{n^2} c_0 \ .$$

The refraction index of each detector is subject to slight variations because of the manufacturing process, aging and material wear. The effective speed of light is therefore a characteristic property for each detector. With exact knowledge of this quantity, timing of both PMs of each detector can be used to calculate the time of flight (sec. 3.2.5) and the position of particle impact (sec. 3.2.6) along each detector.

3.2.4 Effective Attenuation Length

Light traveling through a medium is subject to an attenuation depending on distance traveled inside. For light entering the medium with an initial intensity I_0, the attenuation is given by

$$I(X) = I_0 \cdot e^{-\frac{X}{l}}$$

with the *attenuation length l* depending on the medium. The attenuation length is the distance after which the initial intensity I_0 of the light is decreased by a factor of $\frac{1}{e}$. It was found by L. Schildgen that the attenuation of the SAPHIR detectors is subject to a significant influence of direct light for distances close to the PM. Due to the different contributions of direct and reflected light depending on the distance to the PM, the attenuation length is approximated by [7]

$$I(X) \propto I_{\text{dir}}(X) + I_{\text{ref}}(X)$$

$$= A \cdot \frac{F}{X^2} e^{\left(-\frac{X}{l_{\text{dir}}}\right)} + B \cdot e^{\left(-\frac{X}{l_{\text{ref}}}\right)} \ .$$

The first term describes the attenuation of direct light and is therefore proportional to the solid angle visible by the PM as mentioned before. Attenuation of reflected light is described by second term. As

mentioned before, the distance traveled by the reflected light inside the scintillator is increased by a factor of *n* in comparison to the direct path. Because of this, its attenuation length has to be *shorter* by a factor of $\frac{1}{n}$. Using this relation, the attenuation length of the direct light is expressed in terms of the reflected light, resulting in [7]

$$I(X) \propto A \cdot \frac{F}{X^2} e^{\left(-\frac{X}{n \cdot l_{\text{ref}}}\right)} + B \cdot e^{\left(-\frac{X}{l_{\text{ref}}}\right)}$$

removing one degree of freedom from the equation due to the known refraction index of the scintillator material. This combined expression for the contribution of direct and reflected light is called *effective attenuation length*. During the course of this thesis, it was found that this approximation does not hold when approaching distances to the side of the scintillator which are in the range of the light guide length, which will be discussed in more detail in sec. 4. In this case, the decreased solid angle visible by the PM due to the length of the light guide l_{guide} has to be taken into account, and the approximation for the effective attenuation length is modified to [8]

$$I(X) \propto A \cdot \frac{F}{(X + l_{\text{guide}})^2} e^{\left(-\frac{X}{n \cdot l_{\text{ref}}}\right)} + B \cdot e^{\left(-\frac{X}{l_{\text{ref}}}\right)}.$$

Apart from the contribution ratio of direct and reflected component, the intensity measured at the PM is directly dependent on the initial intensity of light and the attenuation length. The initial intensity corresponds to the ability of the scintillator to convert impinging ionizing radiation into scintillation light, while the attenuation length is strongly influenced by the opacity of the scintillator material. Both of these quantities are again subject to aging and wear and characteristic to each detector. Measuring the effective attenuation length therefore provides a good indicator for the condition of the detectors.

3.2.5 Time Of Flight
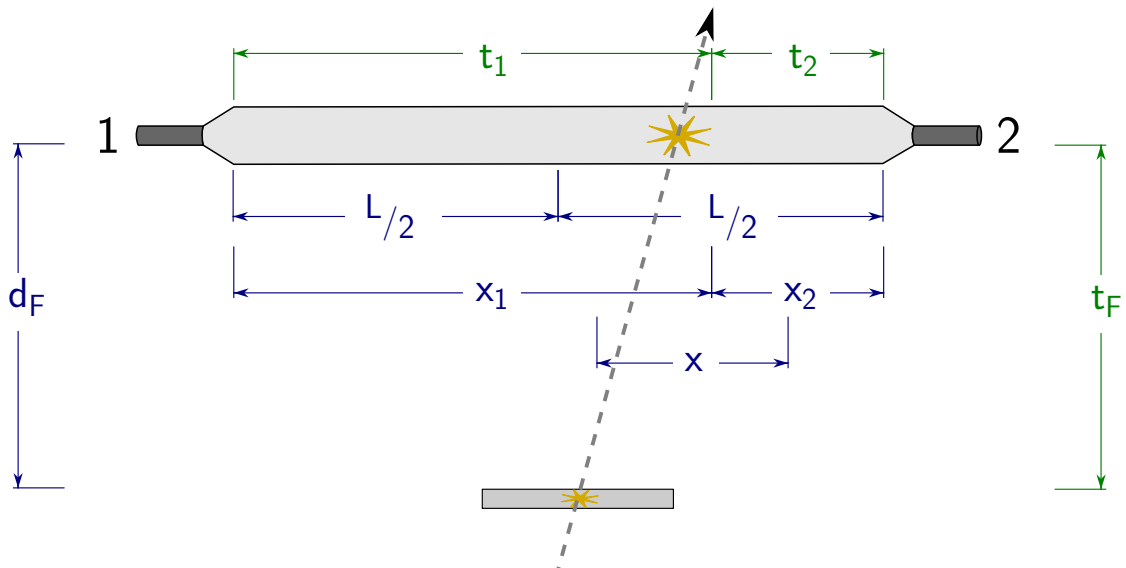
Figure 3.5: Time of flight calculation

If a particle is detected by a trigger detector and the two PMs of a ToF detector, its time of flight and position can be calculated from the TDC information. Such a situation is shown schematically in fig. 3.5. The particle travels a distance d_F between trigger and ToF detector, and produces scintillation light at a distance X measured from the center of the detector. The time difference between passing the trigger and the signal in the PM measured by the TDC is given by the sum of the time of flight t_F and the traveling time $t_{1,2} = \frac{X_{1,2}}{c_{eff}}$ of the scintillation light from its origin to the PM (eqn. 3.1).

$$t_{1,2}^{TDC} = t_F + \frac{X_{1,2}}{c_{eff}} \tag{3.1}$$

The traveling time of the light inside the scintillator depends on the effective speed of light and the scintillator length. With the known detector length L, the distances $X_{1,2}$ traveled along the detector can be expressed by the distance to the detector center. After transformation of eqn. 3.2, the time of flight is given by the average TDC time of both PMs involved and a constant offset given by the length of the detector and its effective speed of light (eqn. 3.3).

$$t_1^{TDC} + t_2^{TDC} = \left(t_F + \frac{X_1}{c_{eff}}\right) + \left(t_F + \frac{X_2}{c_{eff}}\right) \tag{3.2}$$

$$= 2t_F + \frac{1}{c_{eff}}(X_1 + X_2)$$

$$= 2t_F + \frac{1}{c_{eff}}\left(\left(\frac{L}{2} + X\right) + \left(\frac{L}{2} - X\right)\right)$$

$$= 2t_F + \frac{L}{c_{eff}}$$

$$\Leftrightarrow t_F = \frac{1}{2}\left(t_1^{TDC} + t_2^{TDC}\right) + \frac{L}{2c_{eff}} \tag{3.3}$$

3.2.6 Position Calculation

As seen in fig. 3.5, the position X measured from the center of the detector is given by the difference of X_1 and X_2. With the effective speed of light, these are directly proportional to the times $t_{1,2}$. The position along the detector is therefore calculated from the time difference of both TDCs (eqn. 3.1). As a difference is calculated, the trigger times cancel out (eqn. 3.4), and the position along the detector as given by eqn. 3.6 is calculated independent of the trigger time. The effective speed of light is therefore calculated as given in eqn. 3.7. In the first setup of the cosmics test (sec. 4.2), the second relation is used to calculate the effective speed of light of each tested detector. For the second cosmic test setup (sec. 4.3) and the operation of the ToF detectors in the BGO-OD experiment, the first relation is used to

calculate the position of particle impacts.

$$t_1^{\text{TDC}} - t_2^{\text{TDC}} = \left(t_F + \frac{X_1}{c_{\text{eff}}}\right) - \left(t_F + \frac{X_2}{c_{\text{eff}}}\right) \tag{3.4}$$

$$= \frac{1}{c_{\text{eff}}}(X_1 - X_2)$$

$$= \frac{1}{c_{\text{eff}}}\left(\left(\frac{L}{2} + X\right) - \left(\frac{L}{2} - X\right)\right)$$

$$= \frac{2X}{c_{\text{eff}}} \tag{3.5}$$

$$\Leftrightarrow X = \frac{c_{\text{eff}}}{2}\left(t_1^{\text{TDC}} - t_2^{\text{TDC}}\right) \tag{3.6}$$

$$\Leftrightarrow c_{\text{eff}} = \frac{X}{\frac{1}{2}\left(t_1^{\text{TDC}} - t_2^{\text{TDC}}\right)} \tag{3.7}$$

3.2.7 Time Resolution

Calculation of the time resolution is based on a procedure first described by [9], which was already successfully used by [10] and [7] for the characterization of ToF detectors in their theses. At least three detectors in a setup as shown in fig. 3.6 are needed to calculate the time resolution of each detector independent of the trigger timing. Using the Giles-method, the time resolution of detector S is calculated without influence by trigger timing, by using detectors A and B as trigger independent reference. The calculation is based on a combination of averages and differences of the timings involved. The time of flight between the trigger and each detector is given by eqn 3.3 relative to the trigger signal. For the calculation of the time resolution, the constant term corresponding to the detector length and the effective speed of light can be neglected. The previously suppressed term of the trigger time will however have an influence on the time resolution, and therefore has to be taken into account now. The times of flight for each detector are therefore given by eqns. 3.8, 3.9 and 3.10.
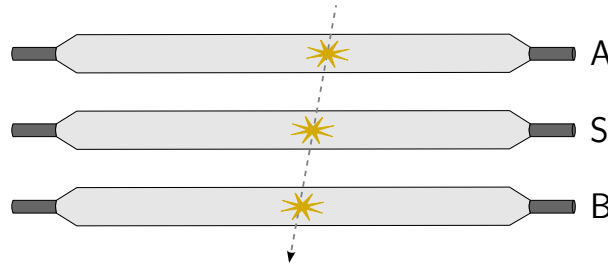
Figure 3.6: The minimal Giles-setup, reworked from [7]

$$T_A = \frac{A_1 + A_2}{2} + T_{\text{trigg}} = T_A^{\text{avg}} + T_{\text{trigg}} \tag{3.8}$$

$$T_S = \frac{S_1 + S_2}{2} + T_{\text{trigg}} = T_S^{\text{avg}} + T_{\text{trigg}} \tag{3.9}$$

$$T_B = \frac{B_1 + B_2}{2} + T_{\text{trigg}} = T_B^{\text{avg}} + T_{\text{trigg}} \tag{3.10}$$

For each detector X, T_X is the time of flight relative to the trigger signal in TDC channels. X_1 and X_2 is the TDC data of the pair of PMs involved. The error ΔT_S is given by Gaussian error propagation (eqn.

3.11)

$$\Delta T_{\mathrm{S}} = \sqrt{\left(\Delta T_{\mathrm{S}}^{\mathrm{avg}}\right)^2 + \left(\Delta T_{\mathrm{trigg}}\right)^2} \tag{3.11}$$

depending on the trigger independent time resolution $\Delta T_{\mathrm{S}}^{\mathrm{avg}}$ of the detector, which is to be calculated, and the error of the trigger timing $\Delta T_{\mathrm{trigg}}$.

$$\begin{aligned} T_{\mathrm{AB}}^{\mathrm{ref}} = T_{\mathrm{B}} - T_{\mathrm{A}} &= T_{\mathrm{B}}^{\mathrm{avg}} + T_{\mathrm{trigg}} - \left(T_{\mathrm{A}}^{\mathrm{avg}} + T_{\mathrm{trigg}}\right) \\ &= T_{\mathrm{B}}^{\mathrm{avg}} - T_{\mathrm{A}}^{\mathrm{avg}} \end{aligned} \tag{3.12}$$

Due to the subtraction of times, the trigger times cancel out. As for all measured timing information, $T_{\mathrm{AB}}^{\mathrm{ref}}$ is a statistically distributed quantity. Therefore, a Gaussian distribution is expected. The distribution of $T_{\mathrm{AB}}^{\mathrm{ref}}$ is called *reference curve*. Its FWHM is one of the quantities needed to calculate the time resolution of S. The offset of the reference curve to zero corresponds to the positioning of the reference detectors relative to each other and is of no further interest for the calculation of the time resolution. $T_{\mathrm{S}}^{\mathrm{ref}}$ (eqn. 3.13) is the time at which the particle crosses detector S, measured by the reference detectors A and B, and is therefore given by the average of T_{A} and T_{B}.

$$\begin{aligned} T_{\mathrm{S}}^{\mathrm{ref}} &= \frac{T_{\mathrm{A}} + T_{\mathrm{B}}}{2} \\ &= \frac{1}{2}\left(T_{\mathrm{A}}^{\mathrm{avg}} + T_{\mathrm{B}}^{\mathrm{avg}}\right) + T_{\mathrm{trigg}} \\ &= T_{\mathrm{AB}}^{\mathrm{avg}} + T_{\mathrm{trigg}} \end{aligned} \tag{3.13}$$

The actual time of particle impact measured by S is given by T_{S}. For each detected signal, $T_{\mathrm{S}}^{\mathrm{Giles}}$ (eqn. 3.14) is calculated from the difference of these average times.

$$\begin{aligned} T_{\mathrm{S}}^{\mathrm{Giles}} = T_{\mathrm{S}} - T_{\mathrm{S}}^{\mathrm{ref}} &= T_{\mathrm{S}}^{\mathrm{avg}} + T_{\mathrm{trigg}} - \left(T_{\mathrm{AB}}^{\mathrm{avg}} + T_{\mathrm{trigg}}\right) \\ &= T_{\mathrm{S}}^{\mathrm{avg}} - T_{\mathrm{AB}}^{\mathrm{avg}} \end{aligned} \tag{3.14}$$

The resulting distribution of $T_{\mathrm{S}}^{\mathrm{Giles}}$ is called *Giles curve*. Its FWHM is the second quantity needed for the calculation of the time resolution. The offset to zero corresponds to the positioning of detector S relative to the reference detectors. If S is exactly centered between A and B, the Giles-curve is therefore equally distributed around zero. For the time resolution, the offset is again of no further interest. Due to Gaussian error propagation, the error of the Giles-curve depends on the errors ΔT_{S} and $\Delta T_{\mathrm{S}}^{\mathrm{ref}}$ (eqn. 3.15)

$$\Delta T_{\mathrm{S}}^{\mathrm{Giles}} = \Delta\left(T_{\mathrm{S}}^{\mathrm{avg}} - T_{\mathrm{AB}}^{\mathrm{avg}}\right) = \sqrt{\left(\Delta T_{\mathrm{S}}^{\mathrm{avg}}\right)^2 + \left(\Delta T_{\mathrm{AB}}^{\mathrm{avg}}\right)^2} \tag{3.15}$$

$\Delta T_{\mathrm{S}}^{\mathrm{avg}}$ can therefore be expressed in terms of $\Delta T_{\mathrm{S}}^{\mathrm{Giles}}$ and $\Delta T_{\mathrm{AB}}^{\mathrm{avg}}$ (eqn. 3.16).

$$\left(\Delta T_{\mathrm{S}}^{\mathrm{avg}}\right)^2 = \left(\Delta T_{\mathrm{S}}^{\mathrm{Giles}}\right)^2 - \left(\Delta T_{\mathrm{AB}}^{\mathrm{avg}}\right)^2 \tag{3.16}$$

The errors of ΔT_{AB}^{avg} and ΔT_{AB}^{ref} are given by eqns. 3.17 and 3.18.

$$\left(\Delta T_{AB}^{avg}\right)^2 = \left(\frac{1}{4}\right)^2 \left((\Delta A_1)^2 + (\Delta A_2)^2 + (\Delta B_1)^2 + (\Delta B_2)^2\right) \tag{3.17}$$

$$\left(\Delta T_{AB}^{ref}\right)^2 = \frac{1}{4} \left((\Delta A_1)^2 + (\Delta A_2)^2 + (\Delta B_1)^2 + (\Delta B_2)^2\right) \tag{3.18}$$

ΔT_{AB}^{avg} is now expressed in terms of ΔT_{AB}^{ref} (eqn. 3.19), which is the FWHM of the reference curve.

$$\Rightarrow \left(\Delta T_{AB}^{avg}\right)^2 = \left(\frac{1}{2}\Delta T_{AB}^{ref}\right)^2 \tag{3.19}$$

Using eqns. 3.16 and 3.19, the time resolution ΔT_S^{avg} of detector S is given by the difference of the squared σ-widths of the Giles-curve and the squared half σ-widths of the reference curve (eqn. 3.20).

$$\Delta T_S^{avg} = \sqrt{\left(\Delta T_S^{Giles}\right)^2 - \left(\frac{1}{2}\Delta T_{AB}^{ref}\right)^2} \tag{3.20}$$

To convert this result from TDC channels to time, all given quantities have to be multiplied by a conversion factor C_{time}. The conversion factor depends on the used TDC, and has to be experimentally calculated. The time resolution τ_S in ns is then given by eqn. 3.21:

$$\tau_S = \Delta T_S^{avg} \cdot C_{time} \tag{3.21}$$

By using Gaussian error propagation again, its error is given by eq. 3.22.

$$\sigma\tau_S = \sqrt{\left(\sigma\Delta T_S^{avg} \cdot C_{time}\right)^2 + \left(\Delta T_S^{avg} \cdot \sigma C_{time}\right)^2} \tag{3.22}$$

$$\sigma\Delta T_S^{avg} = \sqrt{\left(\frac{\Delta T_S^{Giles} \cdot \sigma\Delta T_S^{Giles}}{\Delta T_S^{avg}}\right)^2 + \left(\frac{\frac{1}{2}\Delta T_{AB}^{ref} \cdot \sigma\Delta T_{AB}^{ref}}{\Delta T_S^{avg}}\right)^2} \tag{3.23}$$

The time resolution is completely independent of the trigger, and any of the tested detectors may be used as trigger as well. Therefore, the time resolution measurement with the Giles-method does not rely on external triggering at all. As stated before, the peak offsets of Giles- and reference curves correspond to the positioning of the detectors in relation to each other. Since the time resolution only depends on the FWHMs of these peaks, the detectors may be positioned in arbitrary order above each other. This means that any set of at leas three ToF detectors arranged in arbitrary order and distance above each other provide sufficient information to calculate their time resolution. The Giles-method is therefore ideally suited to calculate the time resolution and is used for the cosmics tests in sec. 4.2 and 4.3.

3.3 Particle Identification

For identification of charged particles with the ToF spectrometer, charge and momentum have to be measured first. This is achieved by track reconstruction, using software by [11], which is still under continuous development. SciFi and MOMO are used for localization of charged particles between target and dipole magnet. If a particle is detected in both detectors, two points of the particle track are given,

completely determining the particle track before entering the magnetic field. Under the assumption that all particles originate close to the target position, a hit in only one of the detectors is sufficient for tracking. For track reconstruction after leaving the magnetic field, multiple driftchambers are placed directly behind the magnet. The magnetic field of the dipole magnet is exactly known by measurements, giving all necessary information for full track reconstruction. A simulated particle track of a proton originating from the target within the BGO ball and passing through the forward spectrometer is shown in fig. 3.7. The charge of the unidentified particle is given by the bend direction in the magnetic
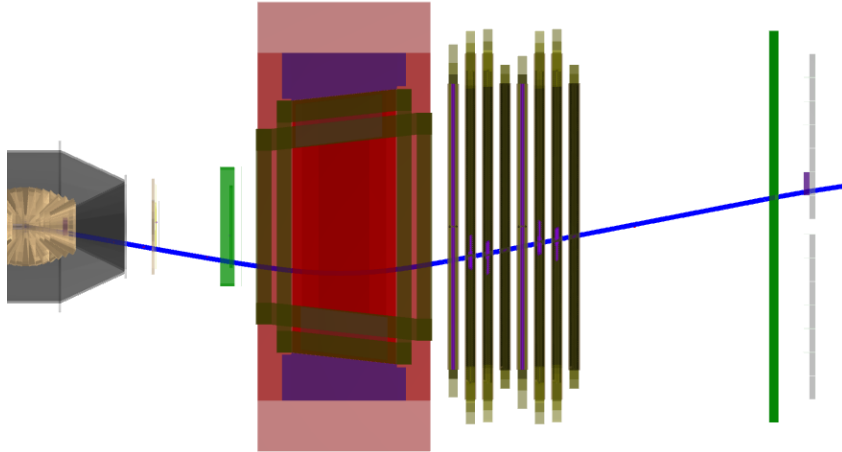
Figure 3.7: Simulated particle track

field and the particle momentum is calculated from the known magnetic field strength and the bend radius of the particle track. The distance traveled by the particle from its origin to the ToF detector is given by the length of the particle track. With the time of particle impact extracted from the ToF detector, the particle velocity is known as well. The time of flight is plotted against particle momentum, as shown for simulated data in fig. 3.8. In this distribution, different particles show a characteristic
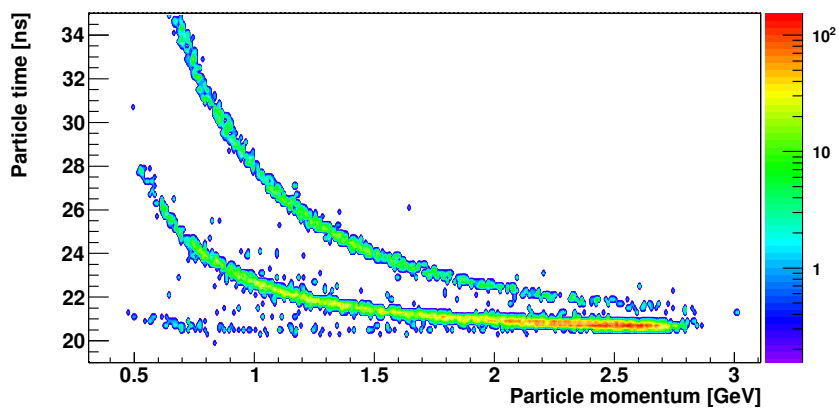
Figure 3.8: Time of flight spectrum from simulated data [12]

dependency between momentum and time of flight, which is used for particle identification. A common property is however the asymptotic behavior for increasing momentum. To distinguish particles in this

range, a good resolution of the time of flight is therefore needed. Simulations by [12] have shown that a resolution of at least around 250 ps is needed for the BGO-OD experiment. In the thesis of L. Schildgen [7], it was already shown that this resolution is not reached with the detectors of the SAPHIR experiment. A sufficient time resolution will however be reached by extending the ToF spectrometer with further detectors from the GRAAL experiment. This extension is being set up at the moment.

Cosmic Ray Test of the ToF Detectors

The characteristic detector properties as described in section 3.2 can ideally be measured using cosmics. As stated in 3.1, at least eight long and fourteen short detectors had to be tested. For this, two different setups were used, both using a fast-slow coincidence circuit, with the deposited charge read out by an ADC and timing information measured by a TDC. A set of four detectors of each type was tested with the first setup, which was already successfully used by Ramseger [10] and Schildgen [7] for the characterization of ToF detectors. After a short section on general remarks concerning both setups (sec. 4.1), the first test setup and its results will be discussed in the section 4.2. Using the results of the first setup as calibration, a second setup achieving a highly increased data rate was used to test all ToF detectors. The second setup and its results will be discussed in sec. 4.3.

4.1 General Remarks

For both setups, a common preparation procedure was used. After preparation of the hardware by renewing the outer wrapping of the detectors, the detector configuration of the first setup as shown in fig. 4.1 was used for HV alignment. The trigger detectors were placed on the side of the detectors near their PMs. An oscilloscope was then connected to one of the PMs of the other side, triggering on a coincident signal in both trigger detectors. The HV of the connected PM was then carefully raised, until a sufficient event rate could be detected by the oscilloscope. This ensures that scintillation light along the detector can still be seen on the other side. This procedure was then repeated for all PMs on both sides of the detectors. The trigger detectors were then placed in the middle of the detectors, and energy distributions with about 2000 events were recorded. The spectra of each pair of PMs were compared, and the HV of individual PMs was increased further until a good overlap of the ADC spectra was achieved. For the short detectors, this HV alignment procedure produced useful HV settings for all detectors on the first try. The long detectors proved to be more problematic. At first, the HV of each PM was again chosen so that signals from the opposing side could still be detected. After the first measurements, saturation effects in the ADC spectra could be observed. These could be traced back to a linear fan-out in the data acquisition chain. For trigger positions close to the PMs, the input range of the fan-out was exceeded. The impact of the resulting plateau region in the ADC spectra on the analysis procedure will be discussed in sec.4.3. The HVs were corrected accordingly and greater care was taken to keep the PM outputs in a usable range. Before each measurement, the ADC pedestals had to be recorded. For both setups, this was done by giving about 100 manual random triggers. Data

acquired with both setups is analyzed using Cern ROOT. Due to the large amount of histograms to be processed, a semiautomatic analysis script for ROOT was developed. Pedestal correction and fitting of all histograms is handled automatically, and where applicable, the same fitting procedures are used for data of both setups. The analysis procedures are discussed in more detail in the following sections.

4.2 The First Setup

In this setup, the detectors to be tested are placed between two smaller trigger detectors with well known properties, as shown in fig. 4.1. Using the available HV supply and readout hardware, four ToF detectors can be characterized simultaneously. A coincident signal in both trigger detectors starts the data acquisition, while the stop is given by a signal in at least one of the tested detectors. As described in section 3.2, the energy deposited by a MIP in a scintillator is proportional to the distance traveled inside the scintillating medium. Since the output signal of a PM is proportional to the energy deposited inside the detector, completely identical particles entering at different angles will lead to different PM outputs. A lower limit for the deposited energy is given for perpendicular trajectories. Selecting such trajectories, all particles travel the same distance in the scintillator and the PM output becomes independent of the incident particle angle. The trigger detectors used have a width of 10 cm and 16 cm. A coincident signal in both triggers thus has a maximum position difference of 13 cm at a distance of about 50 cm, and can therefore be assumed to originate from a perpendicular particle track. The position error along the ToF detectors used in the following calculations is given by the maximum position difference given by the trigger widths. Due to the small surface area of the trigger detectors, only a low data rate can be achieved with this setup. To calculate the effective speed of light and effective attenuation length as described in sec. 3.2, test measurements of at least about five different trigger positions along the tested detectors are needed. At least about 2000 events for each measurement are needed to achieve sufficient statistics. Each of these measurements takes about half a day to complete. This is the main motivation for the use of the second test method described in sec 4.3. Using the first test setup, a set of each four short and long detectors were characterized. Two detectors of each type will be used as reference detectors in the second setup. Therefore, their results will be presented in more detail. Due to the previously mentioned saturation effects for some of the long detectors, their ADC spectra used for the calculation of the attenuation length were only partially usable. The HV settings were lowered accordingly, and a second test run was done.
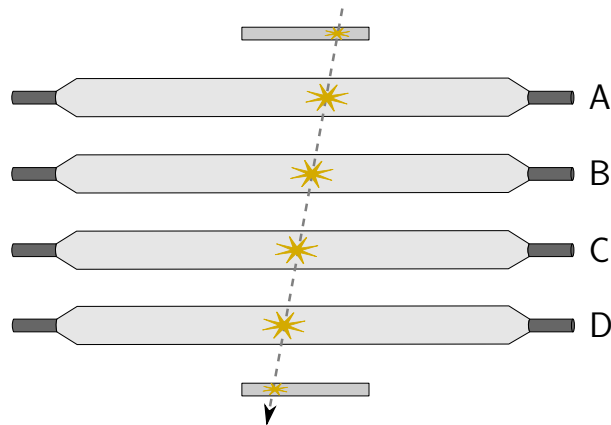
Figure 4.1: The first setup.

Time Resolution

The time resolution for the detectors under test is calculated by using the Giles-method as described in 3.2.7. For each detector, its two nearest neighbors are used as reference detectors. The resulting Giles- and reference distributions for the detectors used as reference for the second setup are shown in figs. 4.2a and 4.2b for SV06, in figs 4.3a and 4.3b for SV08, in figs 4.4a and 4.4b for LH01, and in figs 4.5a and 4.5b for LH05. As already discussed in 3.2.7, offsets from zero correspond to the relative position of the detectors to each other, and are of no further interest for the extraction of time resolutions from the Gaussian fits. Signals in both PMs of all involved detectors are needed. For the outer positions to the left and right, not all signals of one PM are detected by the PM on the opposite side as well. This results in the lower amount of entries in the according Giles- and reference curves. The offsets to zero correspond to the positioning of the tested detector in relation to the reference detectors. Both distributions are fitted with Gaussian functions. The time resolution is then calculated from the widths of the Gaussian fits. The calculation is repeated for each detector and trigger position, and an error weighted mean is calculated as result. The conversion from TDC channels to ns is calculated by applying a conversion factor. Since the same hardware as during L.Schildgens thesis is used, the conversion factor given as [7]

$$0.0509 \pm 0.0008 \text{ ns/Channel} = 50.9 \pm 0.8 \text{ ps/Channel}$$

is used. The resulting time resolutions are listed in tab. A.3 in the appendix. All time resolutions are between 840 ps and 630 ps, with all errors below 23 ps.
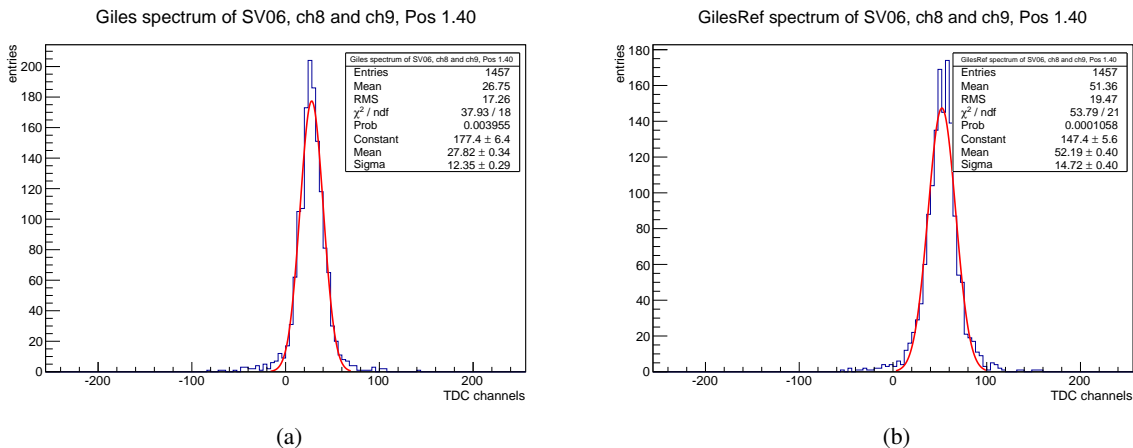
Figure 4.2: Giles - Curve (a) and reference curve (b) of detector SV06

Effective Speed of Light

The effective speed of light is calculated as described in 3.2.7. For each of the trigger positions, the half of the time difference of both PMs of a detector is calculated. The resulting Gaussian distributions for one of the tested detectors are shown in figs. 4.6a, 4.6b and 4.6c for the left, central and right trigger positions. As the triggers are moved from left to right, the traveled distance of light from its origin to the left PM increases, while it decreases for the right PM. This corresponds to the change of the time difference peaks depending on the trigger position, as seen in the figures. Each of the Peaks is fitted with a Gaussian. The trigger position is then plotted against the peak positions. The slope of the fitted linear function then directly gives the effective speed of light in m/ns, as shown in fig. 4.7 for two the short

(a)

(b)
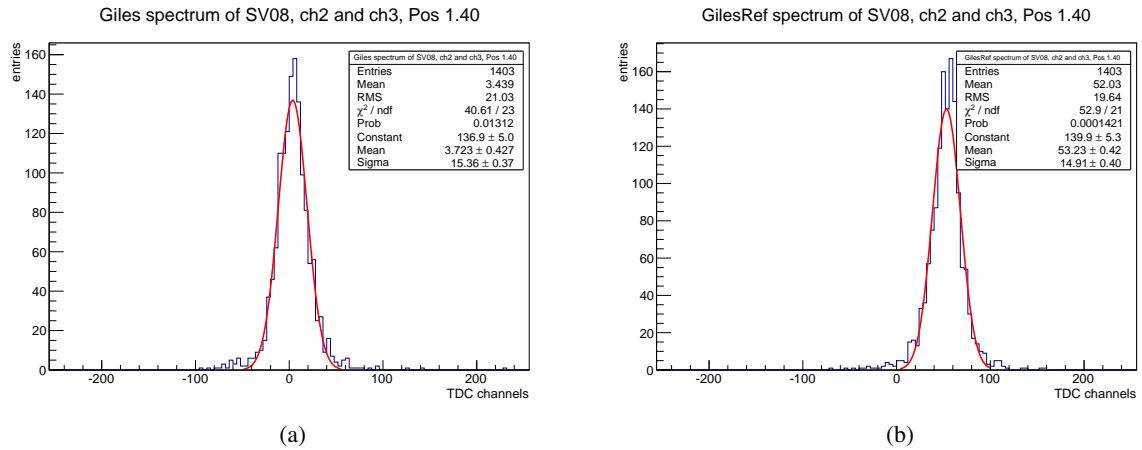
Figure 4.3: Giles - Curve (a) and reference curve (b) of detector SV08

(a)

(b)
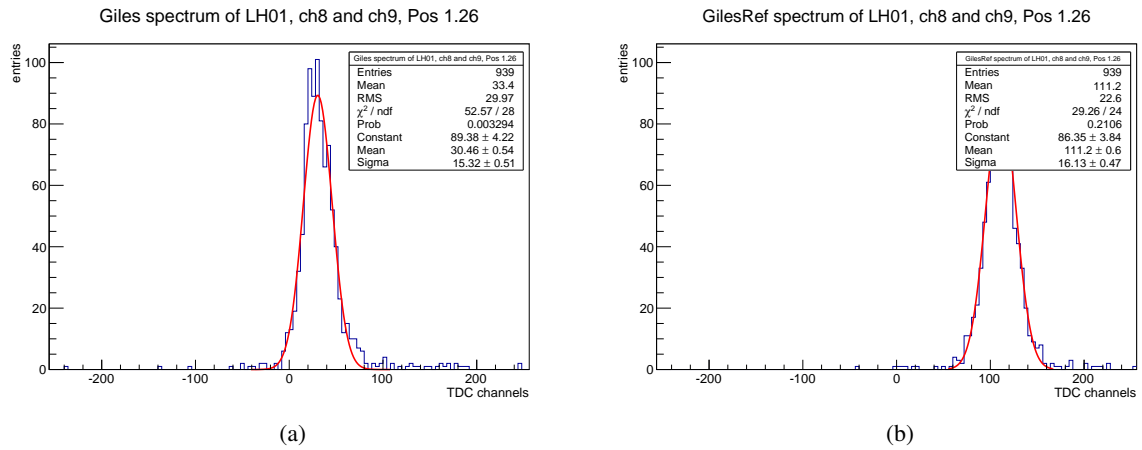
Figure 4.4: Giles - Curve (a) and reference curve (b) of detector LH01

(a)

(b)
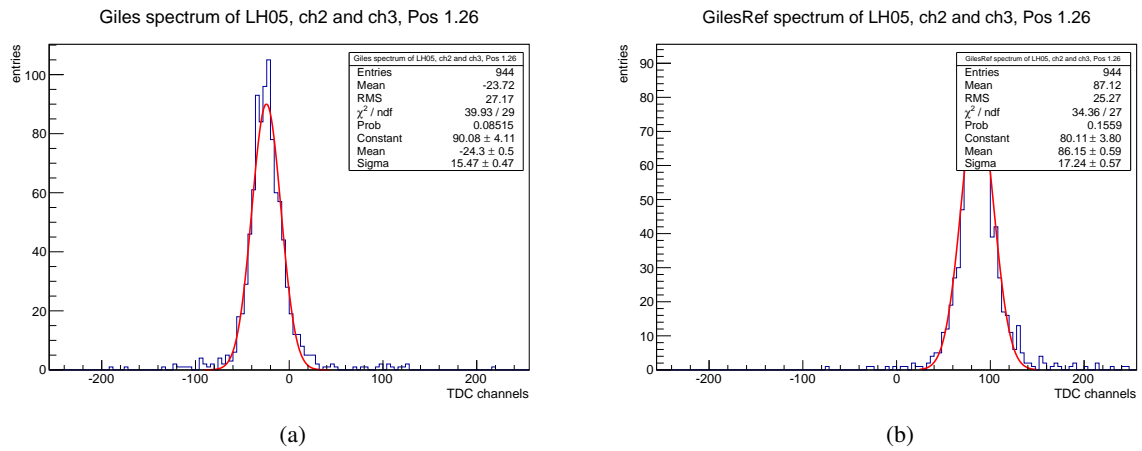
Figure 4.5: Giles - Curve (a) and reference curve (b) of detector LH05

detectors. All data points are situated on a almost perfect line, with no deviation towards the end of the detector. Due to the shorter distance traveled by direct light, a deviation from this line for positions near the PM is expected. The absence of this deviation shows, that at least for the effective speed of light, the influence due to direct light can be completely neglected. Fig. 4.8 and 4.9 show the fits for two of the long detectors of the first and second measurement. Although the influence of the wrong HV setting in the first measurement can be seen in the plots by the slightly larger variation of data points, the resulting effective speed of light was not influenced, as the results only differ minimally within their error range. The table of results (tab. A.2) is again given in the appendix. All values are in a range between 150 cm/ns and 160 cm/ns, with all errors below 4.6 cm/ns.
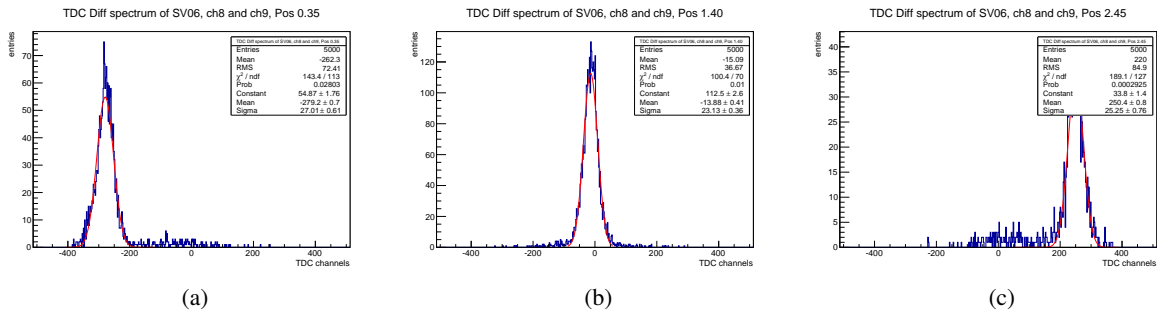
Figure 4.6: TDC spectra of detector SV06 for left (a), middle (b) and right (c) position
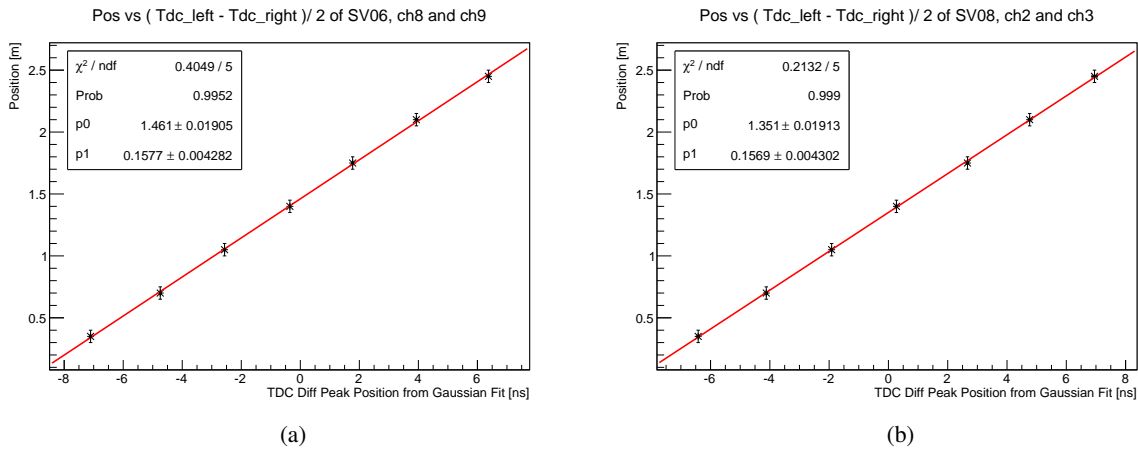
Figure 4.7: Effective speed of light for detector SV06 (a) and SV08 (b)

Attenuation Length

For each set of tested detectors, the ADC pedestals are extracted from a short test run using a random trigger. The corrected ADC spectra for the left, central and right trigger positions for both PMs of a detector are shown in fig 4.10. The change width and peak position for the distributions depending on the distance to the photomultiplier corresponds to the attenuation of direct and reflected scintillation light as described in sec. 3.2.4. Each of the distributions is fitted with a Landau curve. The peak positions extracted from these fits are plotted against the distance to the PM. The data points reproduce the
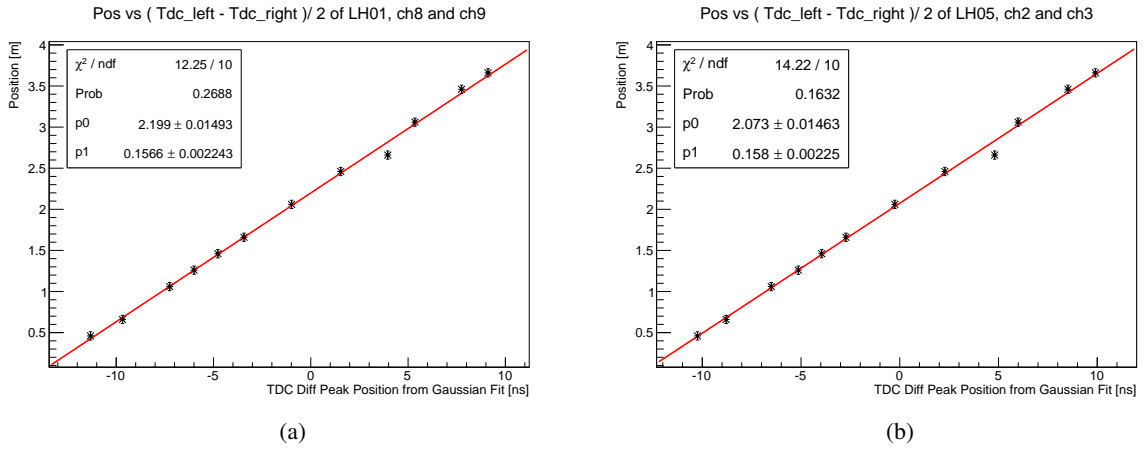
Figure 4.8: Effective speed of light for detector LH01 (a) and LH05 (b), with data of the first measurement
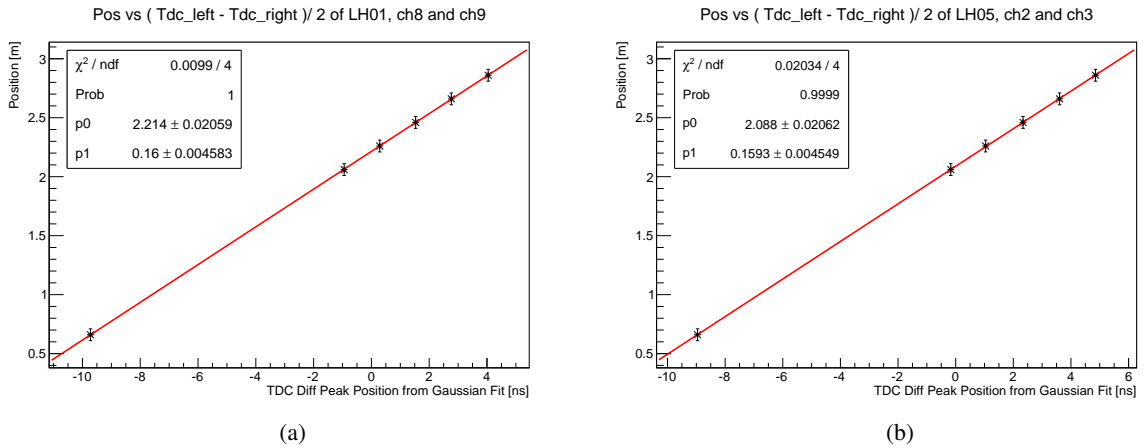
Figure 4.9: Effective speed of light for detector LH01 (a) and LH05 (b), with data of the second measurement

behavior expected form sec. 3.2.4. For trigger positions close to the PM, the direct light dominates the ADC distribution and the data points follow $\frac{1}{x^2}e^{\left(-\frac{x}{l_{\text{dir}}}\right)}$. At distances larger than about 1 m, the influence of the direct light becomes negligible, and the data is described by $e^{\left(-\frac{x}{l_{\text{ref}}}\right)}$. A function of the form

$$f(x) = A \cdot \frac{1}{x^2}e^{\left(-\frac{x}{n \cdot l_{\text{eff}}}\right)} + B \cdot e^{\left(-\frac{x}{l_{\text{eff}}}\right)}$$

is fitted. In all plots for attenuation length within this chapter, the fit parameter $p0$ corresponds to A, $p1$ to B, and $p3$ to the attenuation length in length units of the plot. These plots and the fit results are shown in in fig. 4.11 and 4.12 for two of the short detectors. Figs. 4.13 and 4.14 show the results of two long detectors after the second measurement. The calculated error for the ADC peak position of each data point is obviously too small when considering the deviation of fitted and true peaks as in fig. 4.10. Using these errors for the plots shown in figs. 4.11 to 4.14, the fit of the exponential function does not converge. As a worst case assumption, the peak width of the Landau fits are therefore taken as error along the ADC axis. For both detector types, the fits are in good agreement with the data points. The long detectors show a larger error for the calculated attenuation length due to the lower amount of data points. The effective attenuation length of each detector is calculated from the error weighted mean of both PMs. All results of the tested detectors are given in tab. A.1. The attenuation lengths are in an interval between 1.4 m and 3.1 m, with errors below between 12 cm and 66 cm.
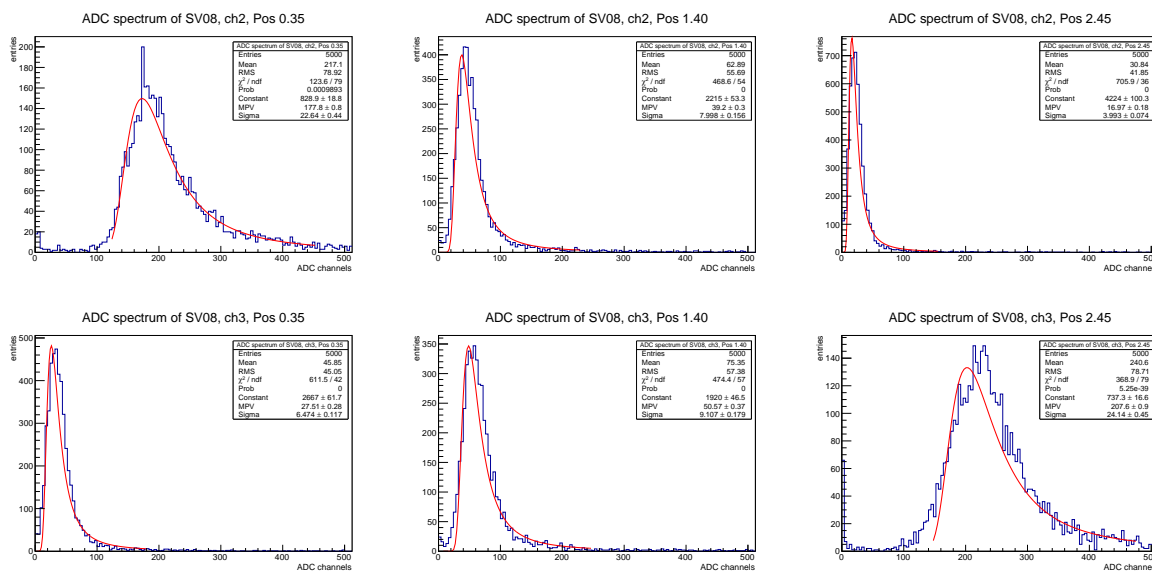
Figure 4.10: ADC spectra of detector SV08. Upper row: left PM; lower row: right PM; Each column for left, middle and right position

Efficiency

The efficiency is given by the ratio of coincident hits in both PMs of a detector and the total amount of trigger hits. This ratio is calculated for each trigger position ad detector, resulting in a efficiency distribution as shown in fig. 4.15 for SV06 and LH01. Ideally, a constant efficiency along the detector is expected. Due to the high HV applied when testing the long detectors, this is nearly reached as shown in fig. 4.15b, with all efficiencies above ~90 %. For the short detector, a significant drop of efficiency
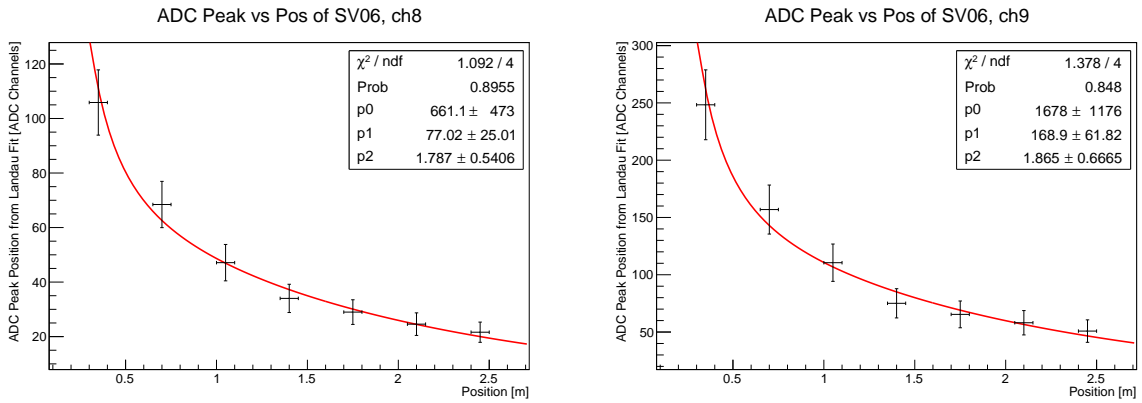
Figure 4.11: ADC peak vs. position, detector SV06
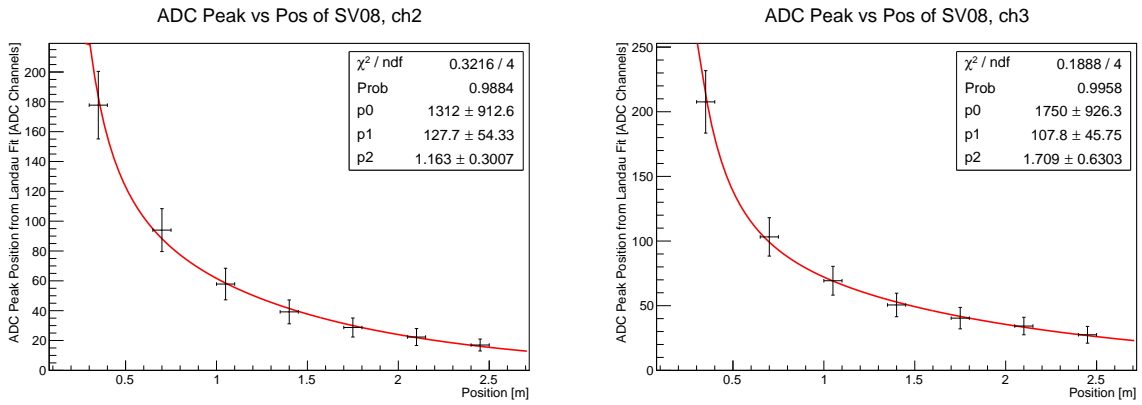
Figure 4.12: ADC peak vs. position, detector SV08
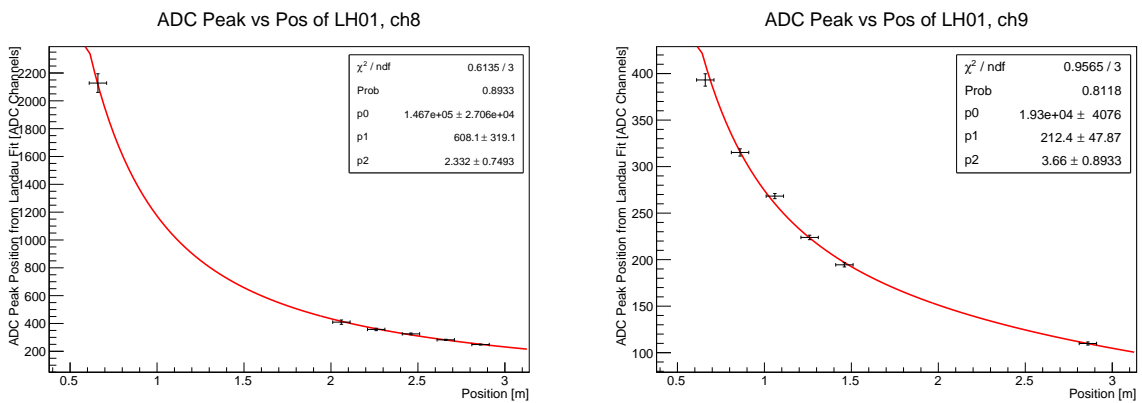
Figure 4.13: ADC peak vs. position, detector LH01, data of the second measurement
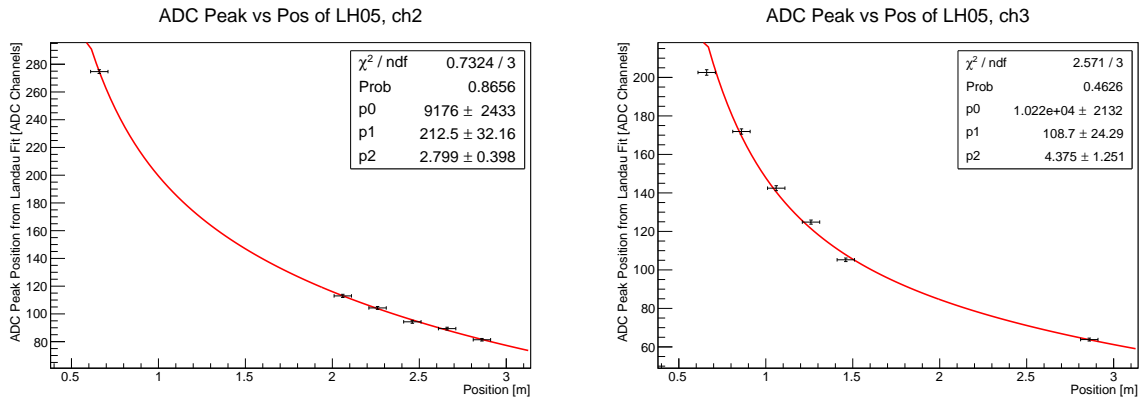
Figure 4.14: ADC peak vs. position, detector LH05, data of the second measurement

towards the side of the detector is seen (fig. 4.15a). The maximum of ~70 % is reached around the middle of the detector, and corresponds to the area where both PMs with the given HV are both able to detect a majority of the incident cosmics. Towards the sides, the opposing PM is not able to detect events producing smaller amounts of scintillation light, and the rate of coincident hits drops accordingly. Raising the HV on both sides would therefore lead to a higher efficiency. Due to time constraints when testing the detectors, an additional test run with higher HVs for the short detectors was not possible. The efficiencies are listed in tab. A.4 in the appendix, with values between 52 % for one of the short detectors, up to 100 % for one of the long detectors.
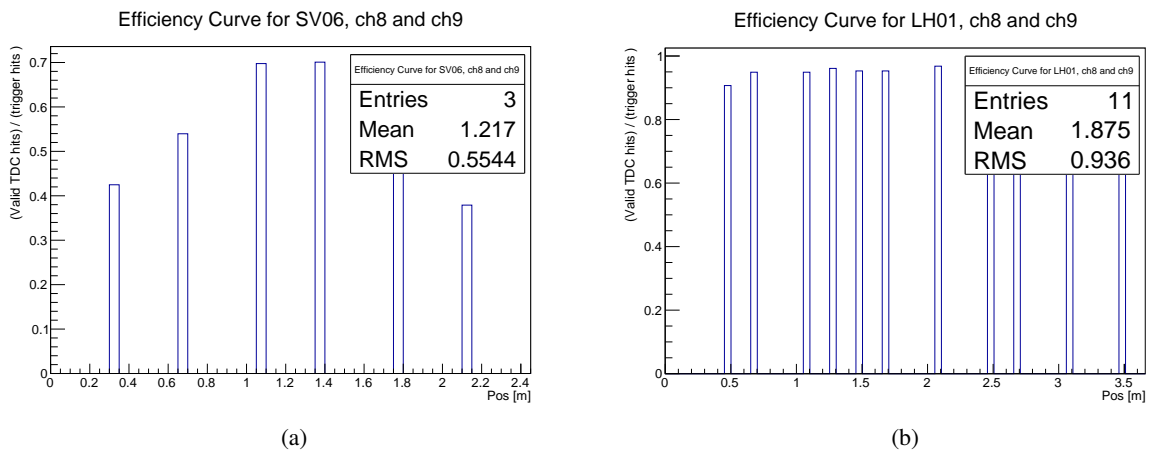
Figure 4.15: Efficiency distribution of SV06 (a) and LH01 (b)

4.3 The Second Setup

With the first setup presented in the previous section, the effective speed of light was measured with good precision as calibration for the second setup. This measurement is now reversed, and the time difference between signals in two PMs of a detector is used to calculate the position of each particle impact. From each set of short and long detectors tested with the first setup, two were selected as reference detectors

and arranged as shown in 4.16 together with the detectors to be tested. Data acquisition is triggered by a coincident signal in all PMs of the reference detectors. In comparison to the triggers used in the first setup, the reference detectors have a much bigger surface area.The tested detectors are covered completely, leading to a higher data rate. The data rate is further increased by the detector width, allowing for a bigger angular distribution of particle trajectories. With this setup, three detectors can be tested simultaneously in less than a day with much better statistics of the data. The changed analysis procedure and its results will be discussed in detail now.
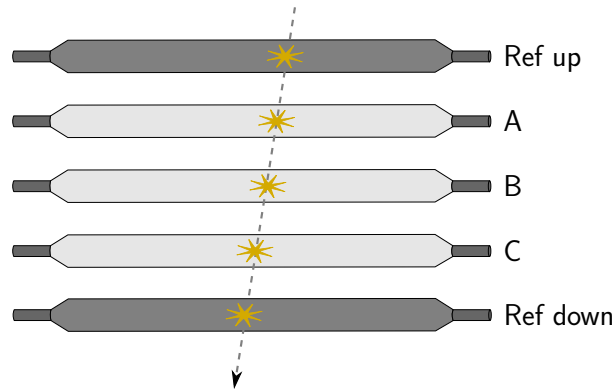
Figure 4.16: The second setup.

Time Resolution

The time resolution is again calculated by the Giles-method. The references for each tested detector are again the two nearest neighbors. Since the influence of the particle distance traveled inside the scintillator is negligible for the timing information acquired by the TDC, no selection on the particle trajectories has to be applied here. The resulting Giles- and reference curves together with Gaussian fits are shown in figs. 4.18, 4.17, 4.19 and 4.20 each for two short and long detectors. The noticeable difference in peak width of the reference curves is caused by the different combinations of Giles-reference detectors used. E.g. during testing the short detectors presented here, SV06 was used as one of the reference detectors for position calculation and triggering, and therefore placed on top of all others. The nearest neighbors for its Giles-reference curve (fig. 4.17b) were therefore SV05 and SV07. Continuing in the permutation of detectors, the nearest neighbors of SV05 were SV06 and SV07, resulting in different offsets from zero, and a different width of the reference curve (fig. 4.18b). The results of the tested set are listed in tab. A.7, and are between 720 ps and 420 ps, with all errors below 12 ps. Due to the increased statistics, almost all fits show significantly reduced errors. In average over all measured detectors, the time resolution error is reduced to about 60 % of the error given by the first setup.

Position and Track Reconstruction

For the calculation of the effective speed of light and the effective attenuation length, the position and direction of each particle causing a hit in the reference detectors needs to be known first. Using the effective speed of light extracted from the first setup and the time difference of each pair of PMs involved, the hit position in each of the reference detectors is calculated as described in sec. 3.2. Together with the known Y-positions of the reference detectors, the full particle trajectory of each event is defined. As explained in sec. 4.2, perpendicular particle trajectories are needed to get PM output signals independent of the particle trajectory. In the first setup, the maximum allowed distance along the X-axis was
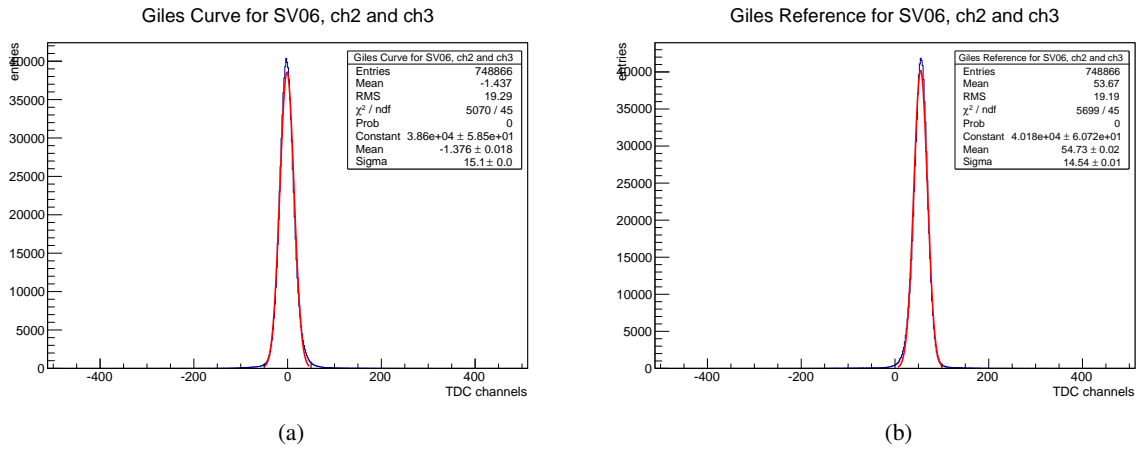
Figure 4.17: Giles - Curve (a) and reference curve (b) of detector SV06
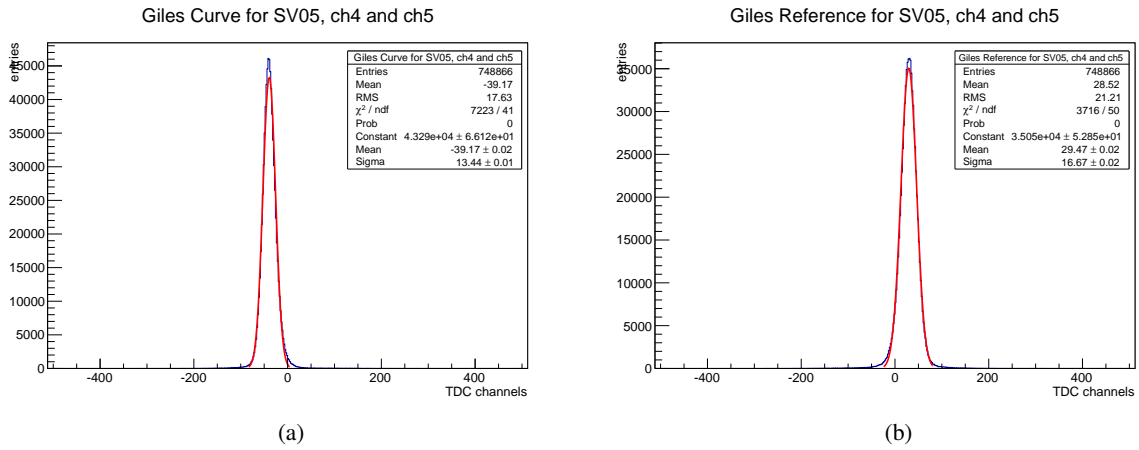
Figure 4.18: Giles - Curve (a) and reference curve (b) of detector SV05
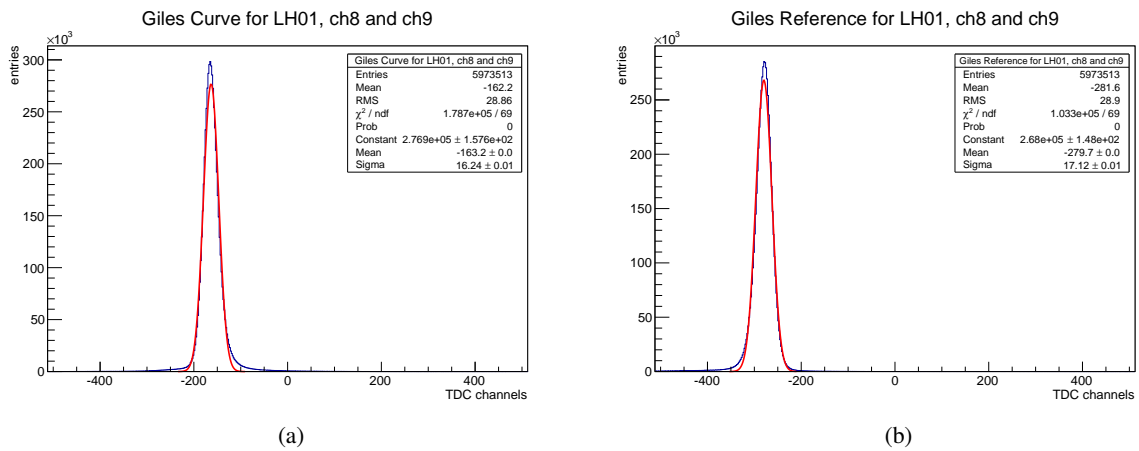
Figure 4.19: Giles - Curve (a) and reference curve (b) of detector LH01

(a)

(b)
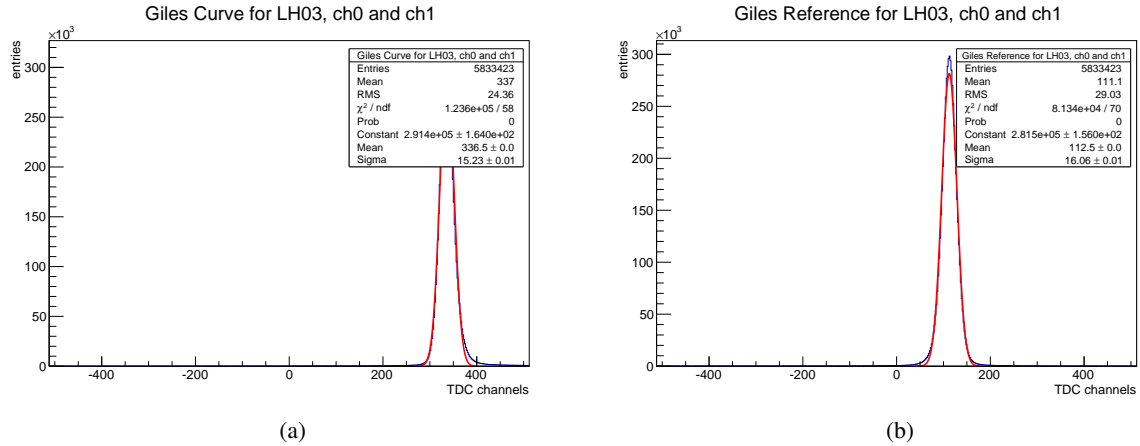
Figure 4.20: Giles - Curve (a) and reference curve (b) of detector LH03

13 cm, given by the geometrical bounds of the trigger detectors used. By choosing a maximum position difference in X-direction of 10 cm between the upper and the reference detector, conditions comparable with the first setup are realized. For each event fulfilling this requirement, the complete particle trajectory is calculated. The expected hit position in X-direction in each tested detector is calculated from the trajectory with the known Y-coordinates.

Effective Speed of Light

The calculation of the effective speed of light is done in analogy to the first setup. For each event with a straight trajectory, the calculated X-position in each tested detector is plotted against half the time difference of both PMs involved. Since the X-position along the reference bars directly depends on the time difference of their PMs, these plots only make sense for the three tested detectors. The resulting distribution is shown in fig 4.21a and 4.22a for one short and one long detector. The expected linear behavior clearly visible. The reason for the more uniform distribution for the long detector is given by the higher HV setting and higher statistics used for its test. The distributions of each detector are projected along the coordinate axis and fitted with a Gaussian. The calculated X-position is then plotted against the peak positions of the Gaussian fits. For the error of the X-position, the maximum allowed distance from the position calculation is assumed, the error of the Gaussian is given by their FWHMs. Resulting plots with applied linear fits are shown in 4.21b and 4.22b for their corresponding detectors. As for the first setup, the effective speed of light is given by the slope of the fit. Due to the position calculation using the reference detectors, positions even closer to the PMs are measured. The slight deviations from the linear distributions of data points in fig. 4.22b in the vicinity of the PMs is caused by the data point which were cut off in fig. 4.22a, and does therefore not correspond to a physical effect. Therefore, even for closer distances to the PMs in comparison to the first setup, no influence of direct light is notable. Results for all tested detectors are given in tab. A.6 in the appendix. The effective speeds of light for all detectors are between 160 cm/ns and 170 cm/ns, with all errors below 5 cm/ns.

Attenuation Length

The ADC pedestals necessary for the correct calculation of the attenuation length are again extracted from a test run with random triggers. Each ADC value is corrected for its pedestal and plotted against

(a) (b)
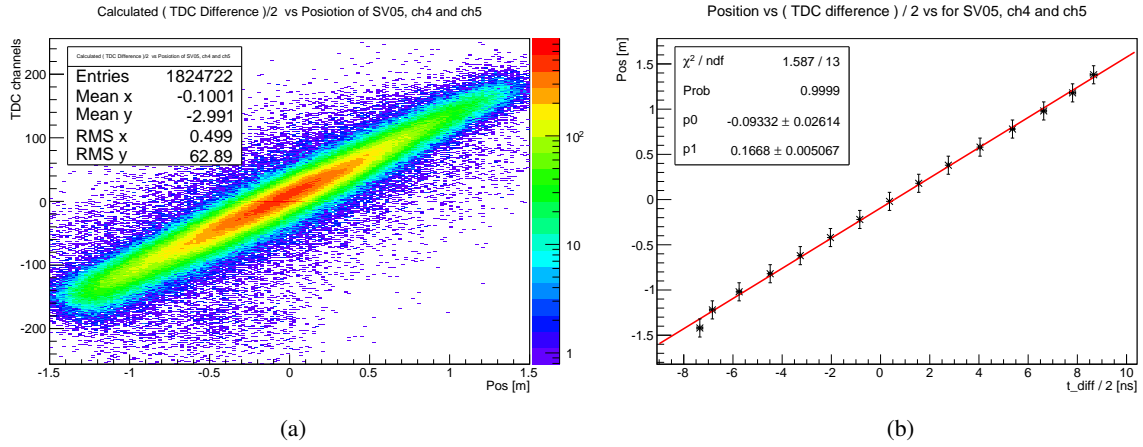
Figure 4.21: TDC distribution (a) and Gaussian peak position of projection (b) for SV05

(a) (b)
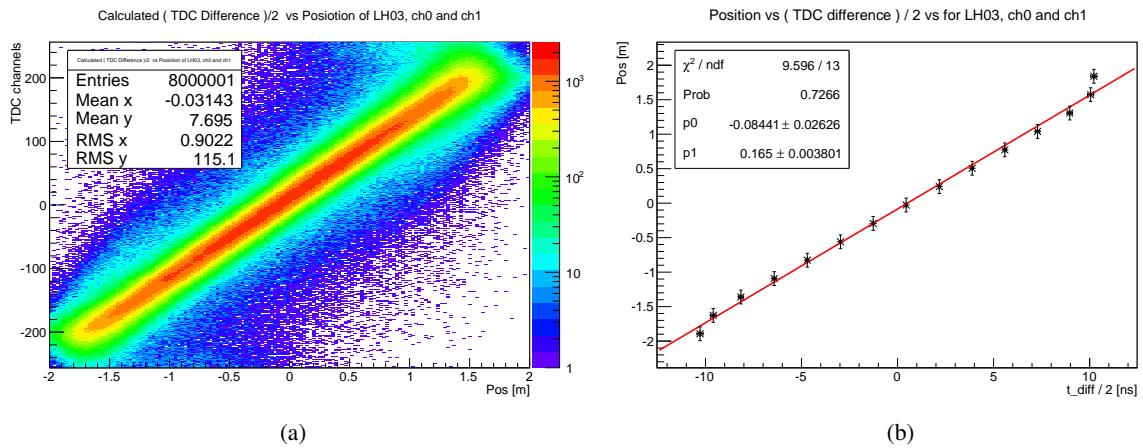
Figure 4.22: TDC distribution (a) and Gaussian peak position of projection (b) for LH03

its calculated X-Position. Since the ADC value is measured independent of the calculated positions, these plots are created for the reference detectors as well. The resulting distribution for the PMs of two short and long detectors are shown in figs. 4.23, 4.25, 4.27 and 4.29 for two long and short detectors. The measurement of the long detectors was taken before the HV values were corrected as mentioned in the previous section (4.2). The plateau-region near the PMs caused by the limited input range of the fan-out can be seen in 4.27. For one PM of the detector shown, an additional bend structure of the plateau is seen. The plateau region and the bend were found to be HV dependent effects and not further investigated due to time constraints. All distributions are again projected along the X-axis and fitted with a Landau curve. Each fitted peak position is plotted against the corresponding X-position as shown in figs.4.24, 4.26, 4.28 and 4.30. From here on, the calculation of the attenuation length is in principle analogous to the first setup. The same exponential function is fitted, and the effective attenuation length of each detector is again calculated from the error weighted mean of the results for both PMs. Non-converging fits when using the peak error of the Landau fits are encountered again, therefore the errors along the ADC axis are again given by the peak widths. However, in comparison to the first setup, the calculation of the effective attenuation length proved to be more difficult. On one hand, the $\frac{1}{x^2}$ term in the fitted exponential makes the fit extremely sensitive for small distances to the PM. Since the distance is calculated from TDC data, even small timing misalignment between the PMs of one detector have a big impact on the fit results. This effect is not noticed in the first setup, since there the distance to the PM is directly measured. For larger distances to the PM on the other hand, the fit becomes very sensitive to the calculated ADC peak position. Depending on the individual HV settings, the ADC distribution remains at a level very close to zero even after subtracting the pedestal. This is encountered e.g. in fig 4.24. When the nearly constant tail of data points to the right is considered for the fit, the attenuation length reaches physically impossible values, and all fit parameters have errors which are several orders of magnitude bigger than the calculated value. An automatic fitting algorithm was developed and is used to encounter these problems. The exponential fit is first applied to all available data points. For each fit parameter, the parameter and its error are stored. The fit bounds are then systematically decreased until each ratio of error to the parameter value drops below preset values. Fits resulting from this procedure are plotted in figs. 4.24, 4.26, 4.28 and 4.30. The resulting effective attenuation lengths for all detectors of are given in tab. A.5 in the appendix. Most values are between 1.7 m and 4 m, with errors up to 1.5 m. In some cases, attenuation lengths of up to 5.4 m are reached with a large error of about 2 m. Most of these cases come from the first test of long detectors with too high HV settings. Averaging over all results, the attenuation length and the error is compatible with the results from the first setup.
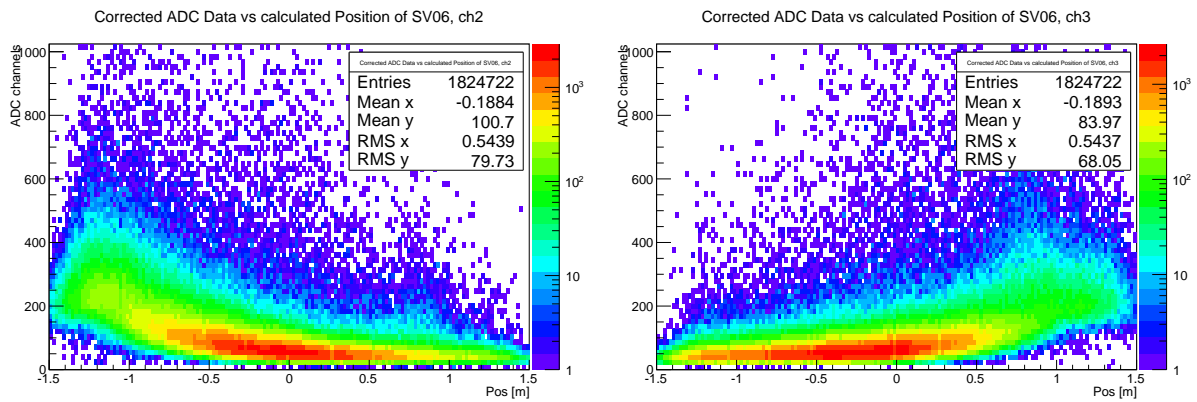
Figure 4.23: ADC distribution of SV06
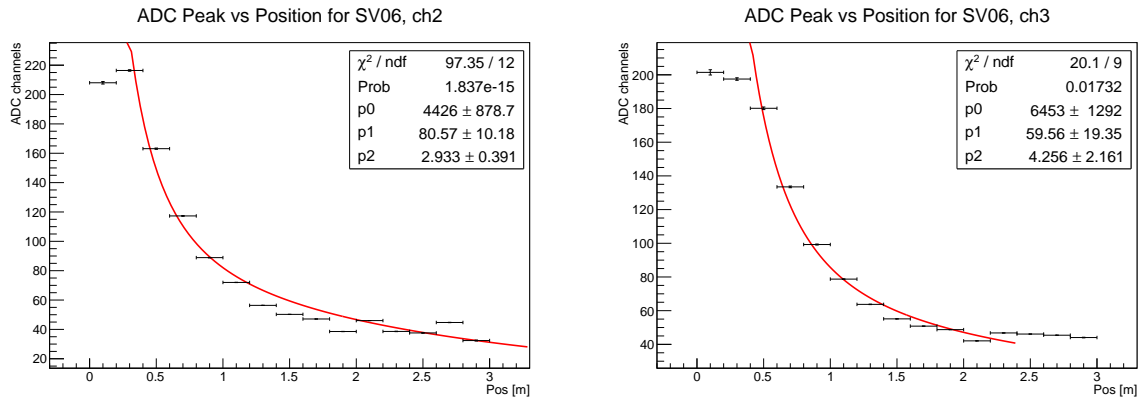
Figure 4.24: ADC peaks vs position for SV06
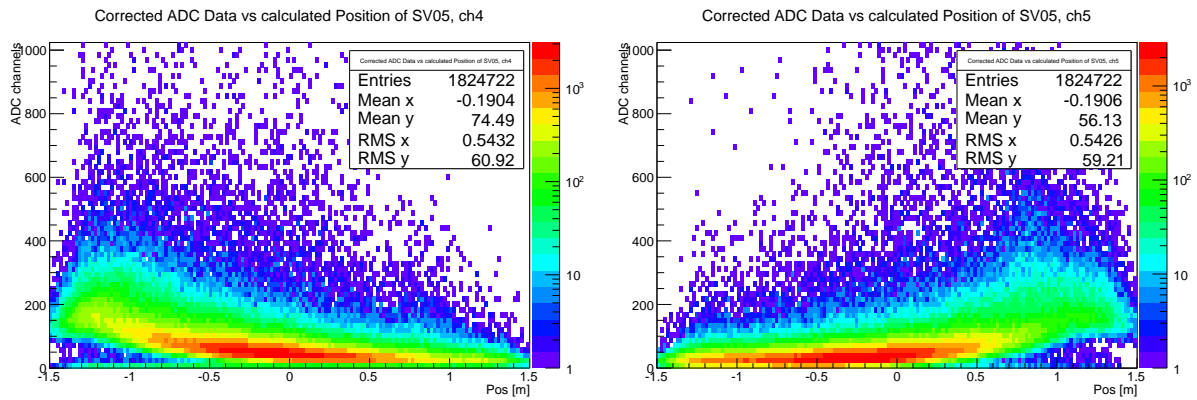
Figure 4.25: ADC distribution of SV05

Efficiency

For the second setup, the efficiency is calculated in similar fashion as for the first setup. The efficiency is given as the ration of coincident hits in both PMs of a detector at each calculated position and the total amount of perpendicular particle tracks within 20 cm. The resulting efficiency distribution for SV07 (fig. 4.31a) is a good example for the effects of asymmetric HV-settings. The left side shows the expected nearly flat behavior with efficiencies around 80 %, rising to above 90 % around the middle. At this position, both PMs are able to detect the majority of the incident particles. Further to the right, the *left* PM is not able to detect all incident particles with the given HV, and the efficiency drops below 40 %. Raising the HV of the left PM would solve this problem, and a nearly constant efficiency above 90 % should be reached for arbitrary positions along the detector. LH04 (fig. 4.31b) shows on the other hand shows a nearly even efficiency distribution above 95 % along large parts of the detector, indicating that sufficient HV was supplied for both PMs to detect particles entering the scintillator on the opposing side. The resulting efficiencies measured with the second setup are listed in tab. A.8. The efficiencies are all in a range between 42 % and 98 %, with the lower values caused by insufficient HV settings when testing the short detectors.
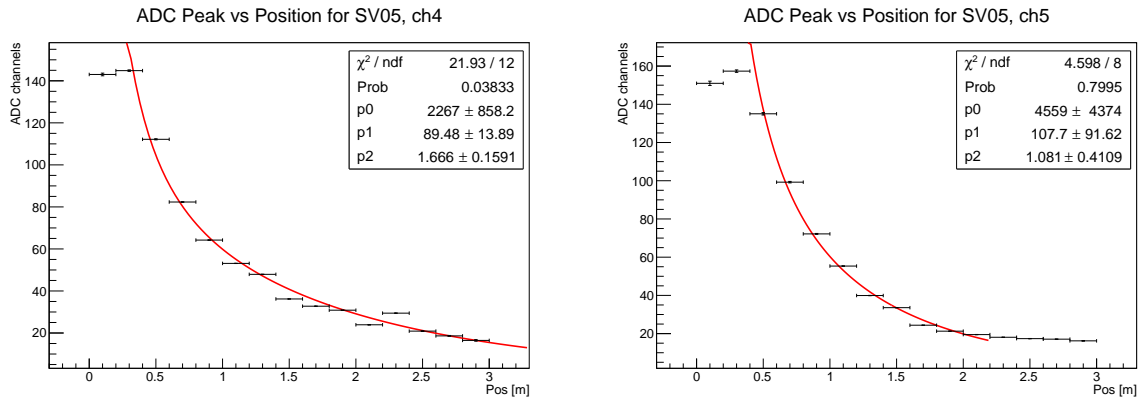
Figure 4.26: ADC peaks vs position for SV05
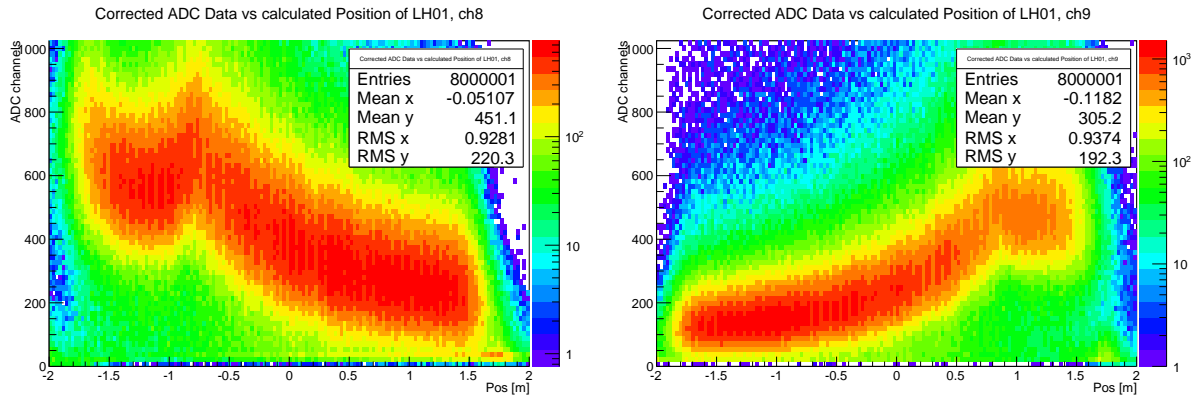
Figure 4.27: ADC distribution of LH01
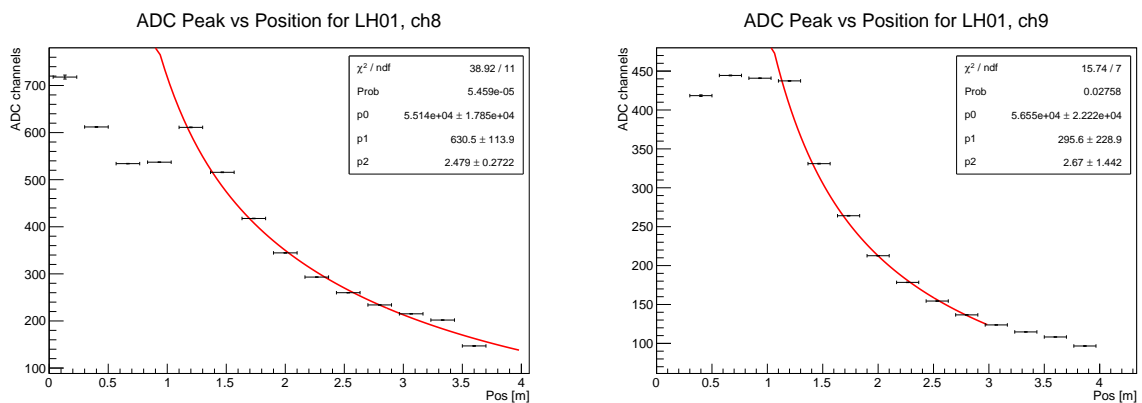
Figure 4.28: ADC peaks vs position for LH01
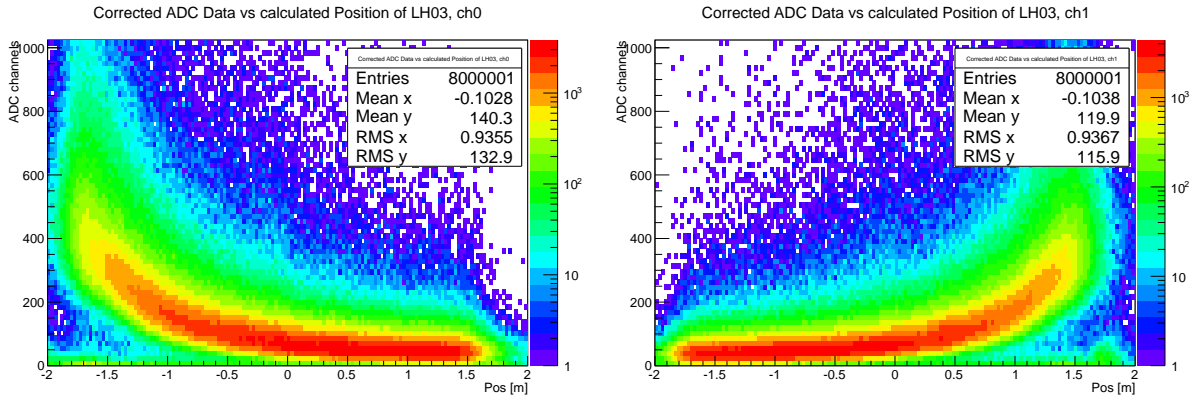
Figure 4.29: ADC distribution of LH03
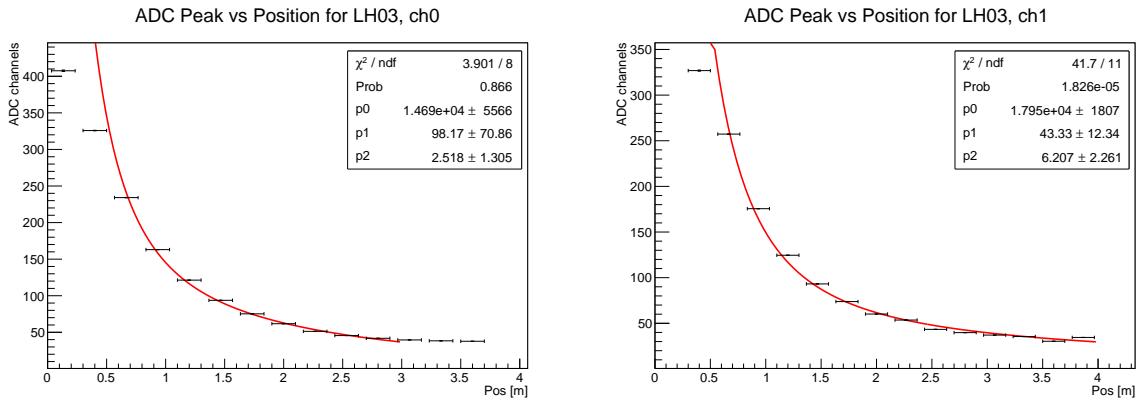
Figure 4.30: ADC peaks vs position for LH03

(a)

(b)
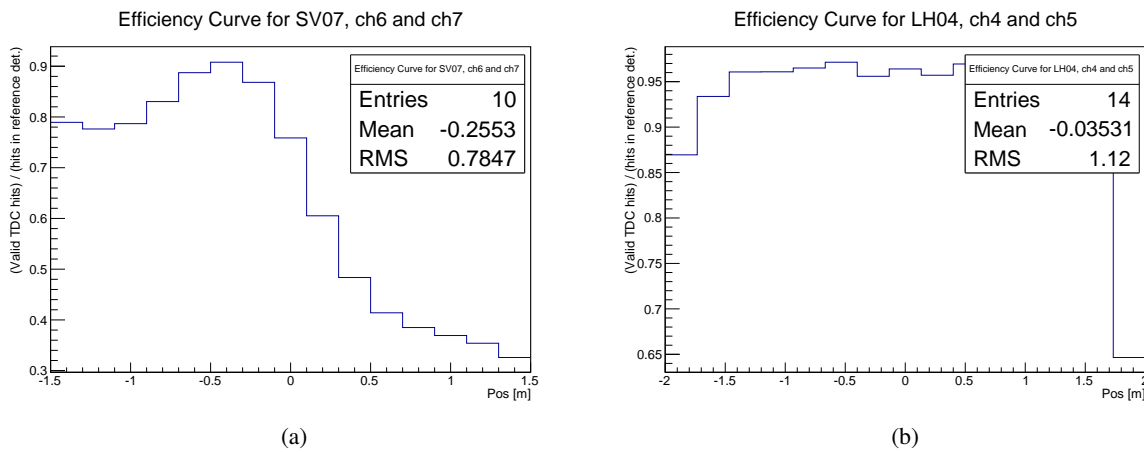
Figure 4.31: Efficiency distribution of SV07 (a) and LH04 (b)

4.4 Discussion of Results

The effective speed of light measured with both setups shows shows a slight deviation outside the margin of error. Averaging over all values measured with each setup, the second setup reaches values which are about 0.80 cm/ns faster than the first setup, which is outside the margin of error. While the first setup shows good compliance with the work of L.Schildgen (around 16 cm/ns) [7, sc12], the values measured with the second setup show a good compliance with the values measured at SAPHIR (between 16 cm/ns and 18 cm/ns, e.g. [2, ba89]). Since the differences between the setups and the reference values by [7, sc12] and [2, ba89]encountered are at most about 1 cm/ns, both setups have proven to deliver reliable results.

For the measured attenuation length, notable differences between the setups occur even for identical detectors. For the reference detectors used during all test runs of the second setup, this applies as well. For identical detectors operated under identical conditions within the tests, differences in the measured attenuation length far outside the margin of error occur. The main cause for this is the extreme sensitivity of the used fit function to small variations of the data pints near the PM, as well as en extreme sensitivity for a flat distribution of data points for larger distances to the PM. The fact that this problem does not occur for the first setup does however not indicate that it is better suited for the measurement of the attenuation length, as the problems are only masked due to the lower statistics and the generally larger distance of the trigger detectors to the PMs. The measured attenuation lengths with and error below 1 m are between 1.2 m and 3.1 m show at least some agreement with the results of [7, sc12] (between 1.5 m and 1.9 m). The results are considerably lower than the results given by [2, ba89] for the SAPHIR experiment (between 600 m and 770 m). Considering the results of [7, sc12], this corresponds however to the expectation, as the attenuation length is expected to suffer the strongest influence due to age and material wear.

The time resolutions for both setups are between about 840 ps and 420 ps and show a relatively large variation over all detectors for both setups. Even the best measured time resolutions are considerably worse than the needed 250 ps (sec. 3.3), making the mentioned extension of the ToF setup inevitable. Time resolutions measured by [7, sc12] were in the range of 430 ps up to 560 ps, so at least the lower values show some agreement, while the larger deviations are expected due to the variation of measured values. As already mentioned, here the second setup reaches a significantly better average error due to the higher statistics.

For the efficiencies between 42 % and 99 % measured with both setups, a strong dependence on the applied HV was noticed for the lower efficiencies. Efficiencies in the range above 90 % are the expectation due to [7, sc12], and are reached in case of sufficient HV settings. Considering all results, the second setup has proven to be a fast and reliable alternative for the characterization of detectors.

All tested detectors of the SAPHIR experiment were found in working condition and installed within the BGO-OD experiment (figs. 3.3, 3.4a and 3.4b). After development of the sampling-ADC readout software discussed in the next chapter (sec. 5), the results of test runs of the complete ToF setup within the BGO-OD experiment are discussed in sec. 6.

Data Acquisition using a Sampling - ADC

During normal operation, the ToF detector is used for time measurement, and therefore only TDC data is required. However, for diagnostic purposes and convenient HV alignment, ADC data is extremely useful. Using an conventional ADC proves to be impractical, as large amounts of delay cables would be needed. Additionally, error diagnosis and HV alignment should both be possible independent of the other components of the BGO-OD experiment, which is not realized by a conventional ADC, as TDC data has to be used for timing. By using a Sampling - ADC (short: SADC), full analog signal shapes of individual PMs are digitized and stored without need for signal delay. Energy and timing information of each digitized signal is gained by pulse shape analysis. Except for an external trigger signal, the SADC operates completely independent, and is therefore ideally suited for this task.

Data acquisition and analysis at the BGO experiment is based on the EXPLORA[1] and CERN ROOT[2] frameworks, which can be easily extended by C++ plugins. Such plugins for readout, correction and analysis of the SADC data were developed and integrated in the EXPLORA framework. After a short introduction on how the SADC works, these plugins will be presented in the second part of this chapter.

5.1 The Sampling - ADC

The SADC used for the ToF setup is a CAEN V1742, capable of storing up to 32 analog input signals at a rate from 1 GSamples/s to 5 GSamples/s. Storage of the analog inputs is realized by four DRS4 Domino Ring Sampling chips within the SADC, each capable of handling 8 of the analog inputs. For each input channel, the analog signal is constantly fed into one of 1024 capacitor cells in a circular sequence at the given sample rate. When an external trigger for data readout is given, the ring sampling sequence is stopped. The charge stored in each of the cells is digitized by internal ADC chips, and data is read out through a VME bus. Such a set of ADC samples is called a *sampling sequence*, giving the SADC its name. Each of these *samples* in a sequence holds a digitized input signal, which was present before the readout was triggered, at a time which remains to be calculated. The time resolution of each sample depends on the *sampling rate*, e.g. the amount of samples acquired per second for each input channel, at which the SADC is operated. For the ToF detector, a rate of 1.0 G Samples/s is chosen to achieve a sampling window size, which is compatible with the timing of the external trigger [8]. This also results in a convenient conversion between samples and time, as one sample corresponds to one ns.

---

[1] Extended Plugable Objectoriented Root Analysis

[2] root.cern.ch/

5.2 Plugin for Raw Data Processing and Correction

The data provided by the raw data readout is not suitable for pulse shape analysis and needs to be processed and corrected first. The necessary steps will be given below.

Cell Offset Correction

The capacitors used for analog signal storage and their PCB readout lines are subject to manufacturing tolerances, resulting in small differences for the charge which is stored and the losses along the way to the ADC chips. Raw data samples for each channel of the SADC are provided in order of the capacitor cells. Plotting the ADC value of each sample against its cell index, this effect is observed as predictable cell wise jitter of the baseline. For a distribution of sampling sequences as shown in fig. 5.2a, the effect is clearly visible. A single sampling sequence of this data set is shown in fig. 5.1a. On the right side of the baseline, a gap of about 30 samples width is visible. These are the last 30 samples of the sequence, and they are discarded on purpose, which will be discussed later in the course of this section. A linear fit is applied to the baseline first. The bins corresponding to each individual cell as shown in fig. 5.2a are projected along the ADC axis. Since for the majority of sequences recorded no signal is present, these projections are sharply peaked. The offset value of each cell is given by the distance between the peak of the projection to the baseline. This calculation procedure is applied to each of the 32 input channels, and the correction values are stored in a database. The first step during data processing is applying the individual offset correction to each cell of all channels. The same data after applying the correction is shown in fig. 5.2b and 5.1b, where the baseline jitter has completely vanished. As the data show in 5.2a and 5.2b is not yet ordered in time, each bin along the X-axis corresponds to an individual capacitor cell of the SADC. In the single sampling sequence, the right side of the gap marks the *start* of the sequence, the *end* is situated on the left side. The start cells of distribution of sequences are statistically distributed along the cell axis. Individual pulses recorded by the SADC after receiving the external trigger are spread out across the whole range of the distribution The position of the gap visible in the single sequence is invisible here, as its position is statistically distributed as well.

Entries	994
Mean x	497.4
Mean y	3632
RMS x	288.5
RMS y	37.62

Entries	994
Mean x	497.4
Mean y	3631
RMS x	288.5
RMS y	24.3

(a)   (b)
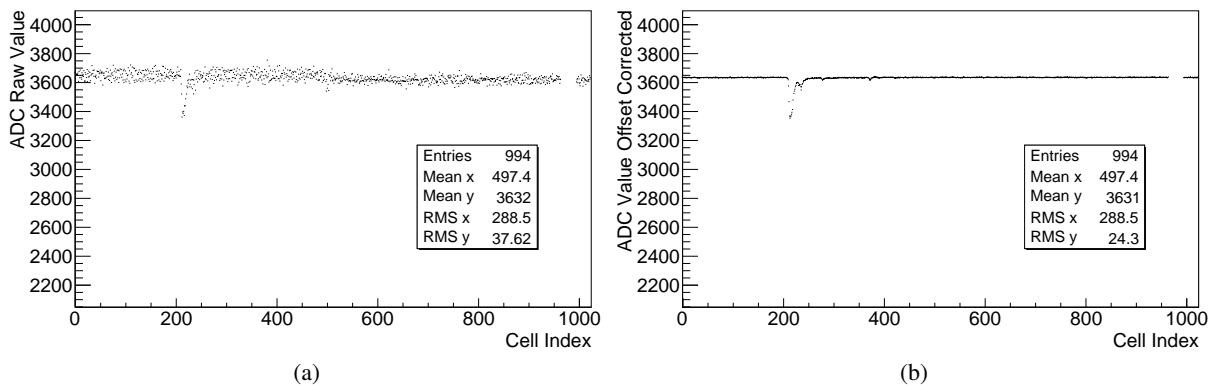
Figure 5.1: Single sampling sequence before (a) and after (b) cell offset correction.

Cell Shift

After applying the cell offset correction, the digitized values of each channel are stored in an array with 1024 entries. This array is filled in order of capacitor cell readout, e.g. the first entry corresponds to the
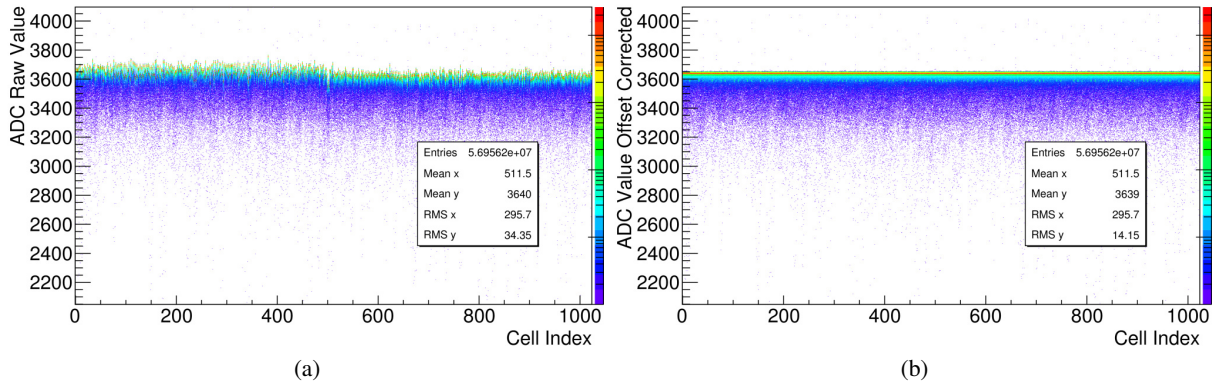
Figure 5.2: Raw data with high statistics before (a) and after (b) cell offset correction.

first cell, and not the first sample of a complete sampling sequence. The cell containing the fist sample is provided by the raw data container. The next step of raw data processing is to apply a shift to the array indices. After this, the first raw data entry corresponds to the first sample of the sequence, e.g. the data now is ordered in time. The same raw data of figs. 5.1b and 5.2b after applying the cell shift are shown in fig. 5.3a and 5.3b. Each bin along the X-axis now corresponds to time in ns after the SADC received its external trigger. For the single sequence, the gap due to the discarded samples is now situated at the correct position at the end of the sequence. The samples on the right side of the gap in fig. 5.1a are now situated at the start of the sample. The discarded samples invisible in fig. 5.1b now overlap at the end of the distribution. An accumulation of previously spread out pulses can be seen. The width and position of this peak in the spectrum are related to the signal propagation time from the PM to the TDC and the times of flight from the used trigger to the ToF wall for all particles involved.
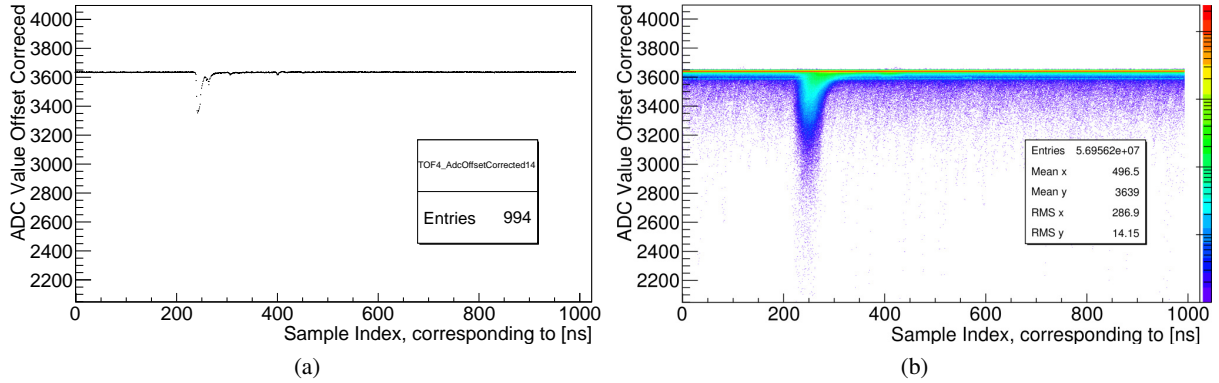
Figure 5.3: Raw data of fig. 5.1b (a) and 5.2b (b) after cell shift

Index Sampling Correction

As mentioned shortly, the last 30 samples of each sampling sequence are discarded on purpose. An enlarged plot of the sampling sequence of fig. 5.1b and a subset of the data of fig. 5.3a both including the last 30 samples are shown in figs. 5.4a and 5.4b. In the former, a strong deviation of the baseline for the last samples is visible and the effect is clearly reproduced by the set of sequences in fig. 5.4b.

The source of the signal jitter is random signal noise after clearing the last cells for recharge in the next coming sampling sequence. This is a known effect for the DRS4 ring sampling chip [13], and cannot be corrected due to the random nature. Since the noise would be wrongly interpreted as a real signal during pulse shape analysis, discarding the last 30 bis is the most feasible solution. The sampling sequence of fig. 5.1b including these samples is shown
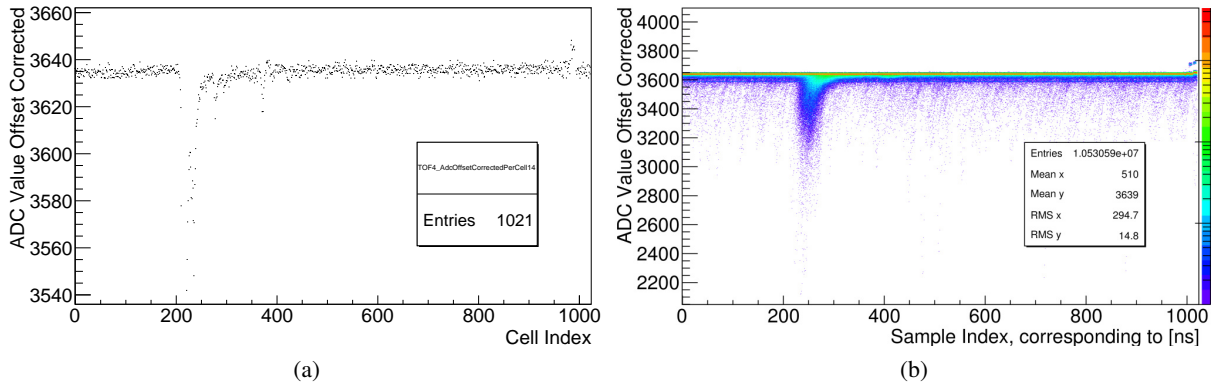
Figure 5.4: Single sample (a) and multiple samples (b) without index sampling correction

5.2.1 Plugin for Feature Extraction

Each time an external trigger is provided, the SADC stores full sampling sequences of all input channels. For data analysis, the energy deposited by particles and its time of impact are needed. These informations are extracted from the full sampling sequences by using pulse shape analysis, also called feature extraction. The feature extraction is done by an EXPLORA plugin written in C++, using the processed and corrected raw data as an input and creating a data container with the needed information as output. Additional input parameters like veto conditions can be easily set by using XML-based configuration files. The necessary steps to extract energy and timing information from raw data will be described in the following. A typical single sampling sequence with a signal present is shown in fig. 5.5. A sequence of samples forming a signal as seen around 250 ns will be referred to as *pulse*. The maximum amplitude of such a pulse will be referred to as *peak*. Additional peaks on the falling edge of a pulse are so called *pileups* and will be discussed in short detail.

Finding the Baseline

The first step in the feature extraction procedure is finding the baseline of each sampling sequence. Calculating the average of all samples was tried out as a fast and easy option. However, each sample deviating from the baseline has an influence on the result of the calculation. Since the start time of each pulse is calculated from the intersection point of a linear fit with the baseline, a shifted baseline will lead to time walk effects. Since the feature extraction does not need to be optimized for speed, this effect is easily avoidable by using the median for baseline calculation. This slows down the calculation of the baseline, but gives reliable results with completely negligible influence by pulses and noise. Fig. 5.5 shows the result of using the median for baseline calculation. Even with a pulse present in the sampling sequence, the calculated and real baseline show a perfect match.
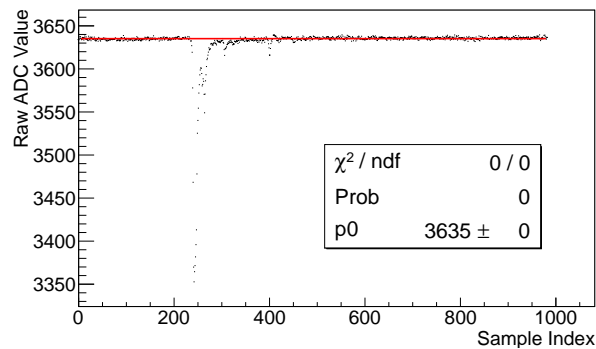
Figure 5.5: Baseline calculated from median for a single sampling sequence.

Edge Detection

After the baseline is subtracted and the resulting sampling sequence is inverted for convenience, the search for pulse edges is started. A quantity sensitive to the change of single sample amplitude is therefore needed. The integral over the sampling sequence rises rapidly as soon as samples above the baseline are encountered. Using this property and applying veto conditions to the result, the rising pulse edges can easily be detected. Thresholds for the baseline and amplitude differences are applied as a first filter for unwanted noise. After this, the integral over the sampling sequence is calculated as described below.

- For samples below the baseline threshold, the amplitude sum is set to -1 to mark it as uninteresting.

- If a sample above the baseline threshold is encountered, the amplitude is added to the sum.

- Following samples with amplitudes higher than the previous and above a threshold for amplitude differences are summed up.

- If a sample with lower amplitude or below the amplitude threshold is found, the sum is zeroed.

- This procedure is repeated until the end of the sampling sequence is reached.

The resulting integrals to each peak of the sequence shown in fig. 5.6a are shown in fig. 5.6b. All peaks of interest are clearly visible. All pulses rising only slightly above the baseline and noise will be filtered out in the following.

Identifying Peaks

The amplitude sums shown in fig. 5.6b alone are not sufficient to distinguish between noise and wanted peaks. Two additional veto conditions are introduced:

- The amplitude sums have to reach a threshold to filter out the small oscillations of the baseline visible in 5.6a.

- A minimum count of samples above a veto threshold around the peak of a pulse is required to filter out sharp noise peaks of single samples.
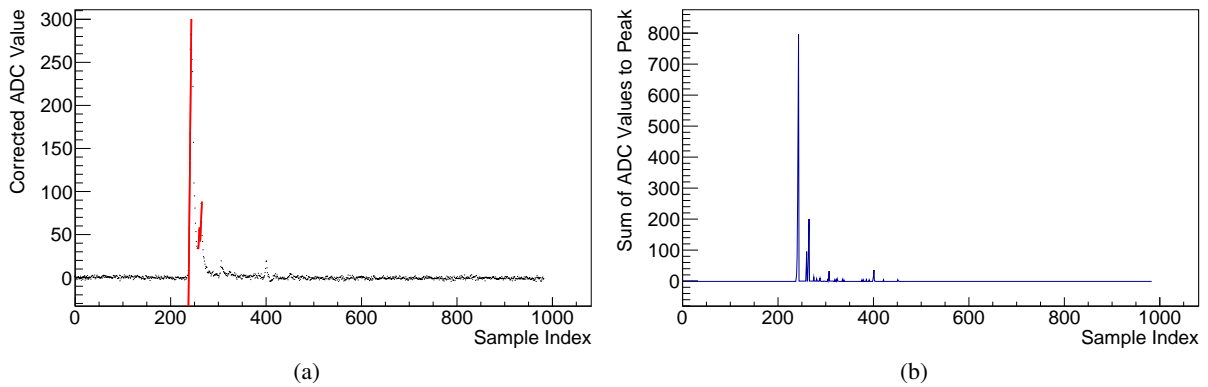
Figure 5.6: Typical sampling sequence (a) and resulting integrals to peak (b)

Calculating Start Times

Start times of the pulses are used for timing information and for calculating the full integral over each pulse at the end of the feature extraction procedure. They are calculated by fitting the signal edges and introducing a further further veto condition.

- For each pulse remaining after applying the previous veto conditions, a linear fit is applied to the data. The fit bounds for each rising edge are given by the spectrum shown in fig. 5.6b. The lower bound is given by the first sample above threshold, the upper bound by the peak position.

- A veto on the slope of the linear function is applied.

- If the fit is successful and no veto given, the start time is given by the intersection of the linear fit with the baseline.

- For pileup peaks on the falling edge of a main pulse, further conditions have to be checked:
  - If the calculated start time of a pileup peak lies before the preceding peak position, the start time of the pileup peak is assumed to be the minimum between preceding peak and pileup.
  - If the fit fails or a veto is given, the minimum is assumed as start time as well.

The resulting fits for the single sampling sequence shown in fig. 5.6a.

Calculating End Times

The end times of each pulse are only needed as upper bound for calculating the pulse integrals. Since the falling slope of the signals approach the baseline asymptotically, the end time does not need to be calculated with a very high precision. The end times are calculated by searching for the first sample below a fraction of the maximum peak amplitude.

- For signals above 100 in arbitrary ADC units, it takes considerably more time until the baseline is approached. For such signals, a fraction of $\frac{1}{5}$ is chosen.

- Signals below 100 arbitrary ADC units reach the baseline faster. A fraction of $\frac{1}{10}$ is chosen for these signals.

However, pileups have to be considered in the calculation of end times as described below.

Pileup Peaks

Pileups are mainly caused by a high rate of incident particles, as the effect was observed in according test runs within the BGO-OD experiment. Although all signal cables are terminated correctly and were checked for damage, signal reflections due to cable damage or poor connection cannot be completely ruled out as source for some of the pileup peaks. The feature extraction plugin is able to handle pileup peaks either as a peak belonging to a separate pulse, or neglecting all occurring pileup peaks on a falling slope completely.

- For each sampling sequence, the start times and maximum of all peaks found are calculated and stored as described before.

- For the first peak found, the end time is calculated.

- If the start time of the next found peak lies between the maximum of the previous (main) peak and its calculated end time, a pileup peak is identified. To avoid a complicated calculation for peaks, which are eventually neglected, the end time of the previous (main) peak is assumed to be the start time of the pileup peak.

- The further handling of the pileup peaks depends on the selected mode of operation:
    - If the pileup peaks are to be identified and stored as hits, the end times of all but the last pileup peak are given by the start time of each following pileup peak. For the last pileup peak, the end time is given by the calculated end time of the main peak.
    - If pileups are to be neglected, their end times do not need to be calculated.

- After all pileups of a main peak are identified and either stored or skipped, the search procedure is started for the next main peak after the calculated end time of the previous main peak.

- The complete procedure is repeated until all main peaks in the sampling sequence are treated.

In both modes of operation, the end time of a first peak is only calculated correctly as value under threshold if no pileup occurs. In the case of rapid succession of first peak and pileup, the length of the first peak will be significantly too short. This can only be overcome by applying much more complicated analysis procedures. It was however shown during test within the BGO-OD experiment, that even after discarding the pileups, a sufficient amount of correct data for HV alignment can be acquired. The results of these tests will be discussed in sec. 6.1 of the next chapter.

Calculation of Peak Integrals and Data Output

After identifying start and end of each pulse, the pulse integrals are calculated by summing the single samples from start to end. During the calculation, each pulse integral is associated to its start time. Data output of the feature extraction plugin are data containers with channel index, start time and pulse integral of each found pulse. These are compatible with other EXPLORA plugins, and can then be associated e.g. to coincident hits of both PMs of a detector.

First Tests within the BGO-OD Experiment

After testing the detectors with cosmics and developing the necessary software plugins for the SADC readout, the complete ToF setup was tested under real operating conditions. The detectors were assembled in two ToF walls as shown in fig. 3.4 and installed within the BGO-OD experimental area (fig. 2.2). SADC data and the analysis plugins described in the previous chapter (5) were used for a first HV alignment. The alignment procedure and its results are presented in the first part of this chapter (sec. 6.1). Geometrical- and timing correlation of both ToF walls will be discussed in sec. 6.2.1. Extrapolated particle tracks are used to give a first estimation of achievable spatial resolution (sec. 6.2.2) and detection efficiency (sec. 6.2.3). The chapter will conclude with presenting a preliminary time of flight spectrum (sec. 6.3) and a short discussion of the results (6.4). All data presented in this chapter was acquired during test runs of the BGO-OD experiment.

6.1 HV Alignment using the SADC

The SADC feature extraction plugin discussed in section 5.2.1 of the previous chapter was used during test beam times for HV alignment between PMs of the individual detectors. Pileup peaks were discarded during data analysis, and resulting distributions for one of the central detectors of ToF4 are shown in fig. 6.1, where the pulse integral of each detected event is plotted against the start time. Most of the entries are accumulated in a narrow region around 300 ns, with its position correlated to the external trigger, and the width given by the effective speed of light and the position of particle impact along the detector. Only few entries are found near zero in direction of the ADC axis, which proves that discarding the pileups is no problem as long as a sufficient amount of data is acquired. Projecting this region of interest along the energy axis, a spectrum of pulse integrals is gained and shown fig. 6.2. The peak position in this spectrum depends on the HV applied to the PM and is used for alignment. In contrast to the cosmics test, arbitrary particle directions are allowed. Additionally and more significant, a relatively large amount of low energetic protons reach the ToF walls, as expected from simulated (fig. 3.8) and supported by measured (fig.6.11) data. The pulse integral spectra are therefore smeared out and shifted to higher values, and only roughly represent a Landau distribution. Since no high precision for the calculation of the peak position is required, a mean value of a Landau and a Gaussian fit is used to calculate the peak position. For HV alignment, the HV is first increased to position the peaks of each detector in the center of the SADC input range. With multiple smaller HV adjustments, the peaks are then brought to a common value within the width of the distribution. The data shown in figs. 6.1 and

6.2 was taken after HV alignment, and therefore a good congruence of peak position in the projections is visible. Although the HV settings of the detectors were aligned, further adjustment of the HV values is needed to reach the intended detection efficiency, as will be discussed in sec. 6.2.3.
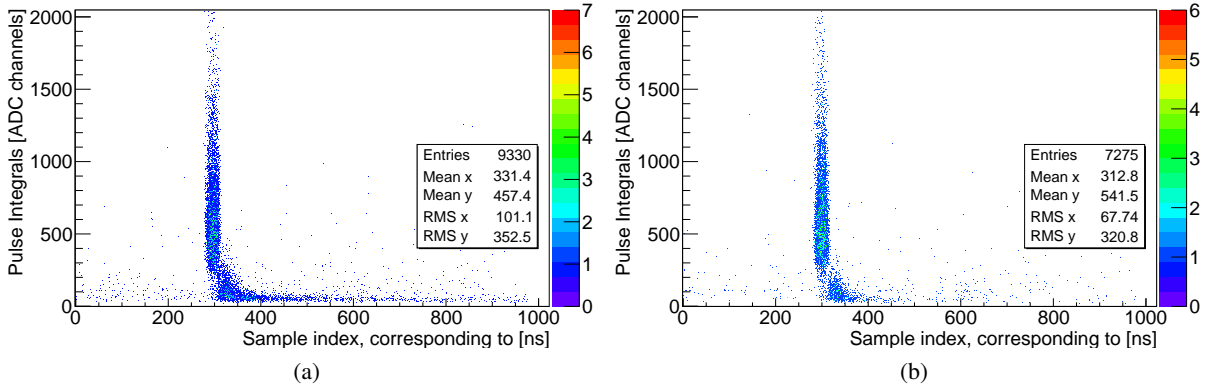
Figure 6.1: Distribution of pulse integrals vs. start times; ToF4 ch17 (a), ch18 (b)
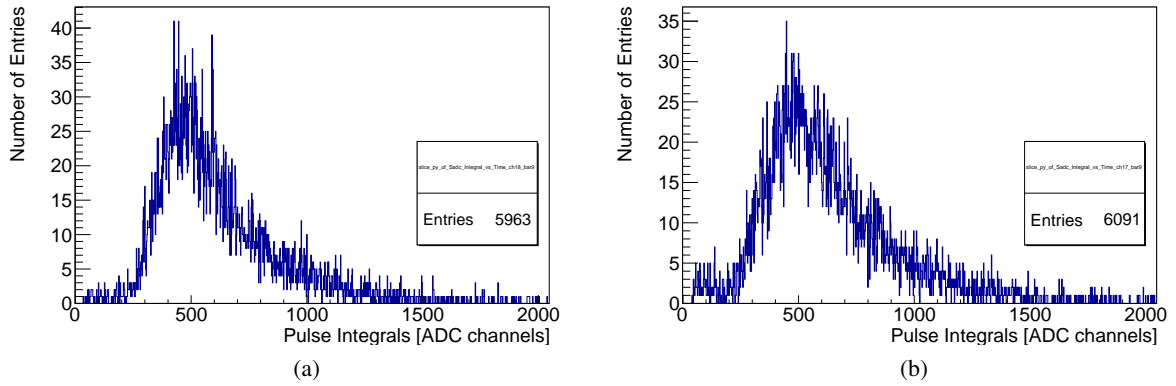
Figure 6.2: Projection along ADC axis; ToF4 ch17 (a), ch18 (b)

6.2 Correlation Analysis

For each particle detected in e.g. SciFi, MOMO and the drift chambers, a complete track is calculated as described in 3.3. Since the tracking is based on multiple independent detectors, a complete particle track will on one hand correspond to a real particle with relatively high probability. On the other hand, the tracking algorithms are still under continuous development, and all tracking data has to be considered as preliminary. Particle tracks have to be extrapolated from their last measured position and direction at the drift chambers, which introduces an additional uncertainty. Even small errors in track position and direction will therefore have a large impact on the calculated position at the ToF walls. In the course of this section it will however be shown that even the preliminary tracking proves to be reliable.

Information about the spatial resolution of the ToF detector is extracted from correlation between positions measured in each ToF wall, as well as from correlation between positions measured by the ToF detector and extrapolated particle tracks. Considering the correlation between measured position and

time at each ToF wall, it will be shown that an exact offset correction between the TDCs is still necessary. Comparing the amount of extrapolated tracks entering the detector and the amount of coincident detected particles within a maximum distance around the track, a first estimation of detection efficiency is extracted.

6.2.1 Geometric Correlation between ToF Walls

Position

The position along the detectors is calculated from TDC data and the effective speed of light, while the coordinate perpendicular to the detectors is chosen in the center of the detector. For each coincident hit in both ToF walls, the position difference is calculated, resulting in the distribution shown in fig. 6.3. A relatively sharp peak is situated near the center of the coordinate system, showing that a majority of the hits detected in both ToF walls are correlated in their measured position.
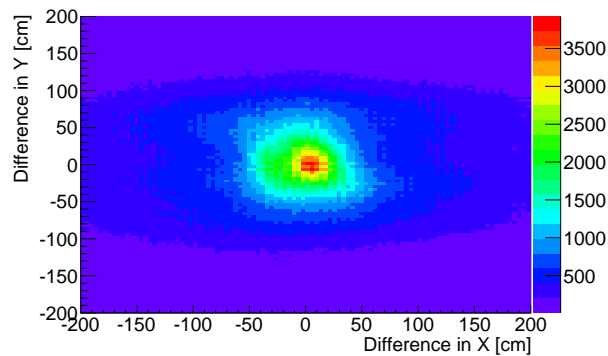
Figure 6.3: Geometric correlation of hits in both ToF walls.

Timing

An offset correction to each TDC has to be applied to compensate differences in cable lengths and electronics. During the test runs, this offset correction was not yet applied, resulting in errors for all TDC data and the positions calculated from these. The effect of TDC misalignment becomes clear when considering fig. 6.4. For each coincident hit in both ToF walls with a position difference less than 40 cm in X- and Y-direction, the time difference ($t_{\mathrm{ToF3}} - t_{\mathrm{ToF4}}$) is plotted against the detector position of ToF3 (fig. 6.4a) and ToF4 (fig. 6.4b). The visible peaks in the hit distributions show that there is a correlation, although offsets of the peaks from zero are visible as well. A slight regular deviation from zero is expected due to the position difference of ToF3 and ToF4 along the beam line. For particle trajectories with larger distances from the beam axis, this effect should become even more prominent, as more particles will enter the ToF detectors at larger angles, thereby increasing the time of flight between the ToF walls. Time differences due to the position of the ToF walls should happen in a predictable manner. The irregularities and the offset values of up to a few ns are therefore mainly caused by the misalignment of TDC pairs, as the X-coordinate in ToF3 and the Y-coordinate in ToF4 are given by the time differences, and wrong combinations of hits in ToF3 and ToF4 fall in the coincidence window of 40 cm.
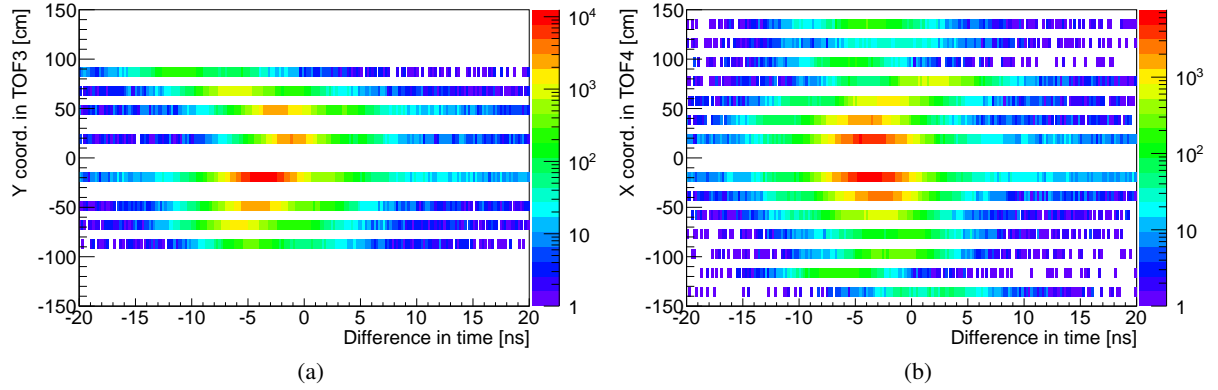
Figure 6.4: Correlation of time difference between ToF walls and detector position in ToF3 (a) and ToF4 (b).

6.2.2 Geometrical Correlation with Particle Tracks

For each extrapolated particle track in coincidence with a hit in one of the ToF detectors, the difference of the X- and Y-coordinates is calculated and plotted. The resulting distributions of position differences are shown in figs. 6.5a and 6.5b for ToF3 and ToF4. The width of these gives a first estimation about the achievable spatial resolution of the ToF detector. Both distributions are projected in X- and Y-direction, as shown in figs. 6.6 and 6.7. Due to the orientation of the ToF detectors (fig. 3.4), the X-coordinate of ToF3 and the Y-coordinate of ToF4 are the coordinate along the detector calculated from TDC data. The other coordinate is given by the position of each individual detector. In the distribution of position differences in detector direction for ToF3 (fig. 6.6a), two peaks are clearly visible, which is in complete contradiction to expectation. The left peak has only a slight offset towards zero, and corresponds to correct coincidences between extrapolated particle tracks and measured position. The right peak however indicates that a significant amount of particles are measured in coincidence with a particle track, but with an constant negative offset in measured position (due to ($X_{track} - X_{ToF}$)). The analogous distribution of ToF4 (fig. 6.7b) shows a hint of a second peak around -40 cm as well, while the position differences perpendicular to the detectors (figs. 6.6b and 6.7a) show no such effect and only have one peak near zero. All extrapolated particle tracks entering the ToF detectors (fig. 6.8) show an even distribution, which rules out the tracking as the source of the effect. Since only the distributions involving TDC data are affected, the cause is probably given again by misalignment of the TDCs. The exact cause could however not yet be determined. Gaussian peaks are fitted to the data, and the spatial resolution is given by the sigma widths. Perpendicular to the detectors, ToF3 and ToF4 reach spatial resolutions of 9.98 ± 0.06 cm and 9.47 ± 0.05 cm. Along the detectors, the expectation is estimated by assuming a worst-case time resolution of ~0.80 ns and an effective speed of light of ~16 cm/ns. The time resolution is calculated for the average time of two PMs. As the position is calculated from the difference, an additional factor of 2 has to be applied. The result is an expected spatial resolution of about ~26 cm. The central peak in the according distribution of ToF3 with a width of 25.3 ± 0.5 cm corresponds relatively good to this worst case assumption. For ToF4, the fit gives a width of 20.00 ± 0.14 cm, which is slightly better.

6.2.3 Efficiency

The efficiency of a detector is defined as the ratio of particles entering the detector and the count of particles detected. No requirement for the correct position is included in this definition yet. The count
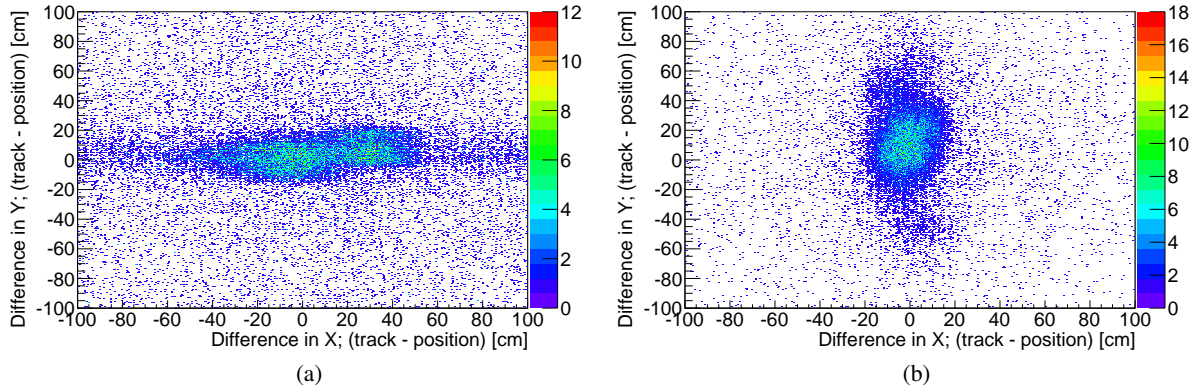
Figure 6.5: Correlation of extrapolated tracks and measured position at ToF3 (a) and ToF4 (b).
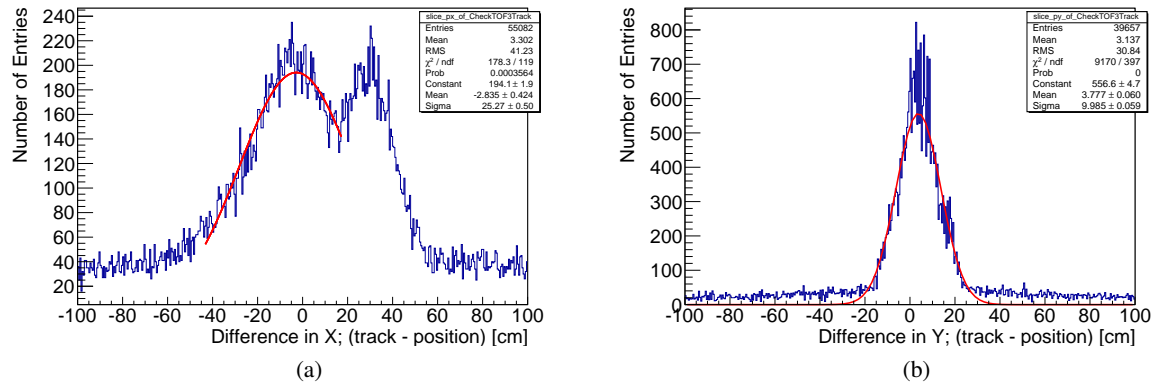
Figure 6.6: Projection and fit of data from fig. 6.5a along Y (a) and X (b) direction.

of particles entering the detectors is given by the extrapolated particle tracks. For each extrapolated track, an accidental coincident hit at an arbitrary position along the detector would still contribute to the efficiency. This has to be corrected by selecting only particle hits detected at the correct position along the detectors. Considering the results from the geometric correlation with extrapolated tracks, the maximum allowed position difference in X and Y direction is chosen as 20 cm. Measured positions outside this range are considered as accidentals and therefore must not contribute to the efficiency. The efficiency is then given as the ratio of tracks with a coincident hit at ToF3 (fig. 6.9a) and ToF4 (fig. 6.9b), and the total amount of extrapolated tracks entering ToF3 (fig. 6.8a) and ToF4 (fig. 6.8b). A bin size of 20×20 cm is used for calculation of the ratio histograms, resulting in a coarse efficiency distribution for ToF3 (fig. 6.10a) and ToF4 (fig. 6.10b). The data shown was acquired during the first test of the complete ToF setup and a conservative HV setting for all detectors was used. During the test run, the dipole magnet was switched on, therefore the calculated tracks show a broad spread in X direction. The distributions of coincident hits in ToF3 (fig. 6.9a) and ToF4 (fig. 6.9b) both are uneven. In the upper part of ToF3, the hit distribution shows a lack of entries on the right. This corresponds to a insufficient HV setting for the left side of the corresponding detectors, as it was already encountered and explained in secs. 4.2 and 4.3. For ToF4, a drop in the amount of entries to the sides is visible, with a gap on the left side. The gap was caused by a malfunction in the HV supply of the corresponding detector during the test run, and the drop of entries to the sides corresponds to an insufficient HV setting again. This
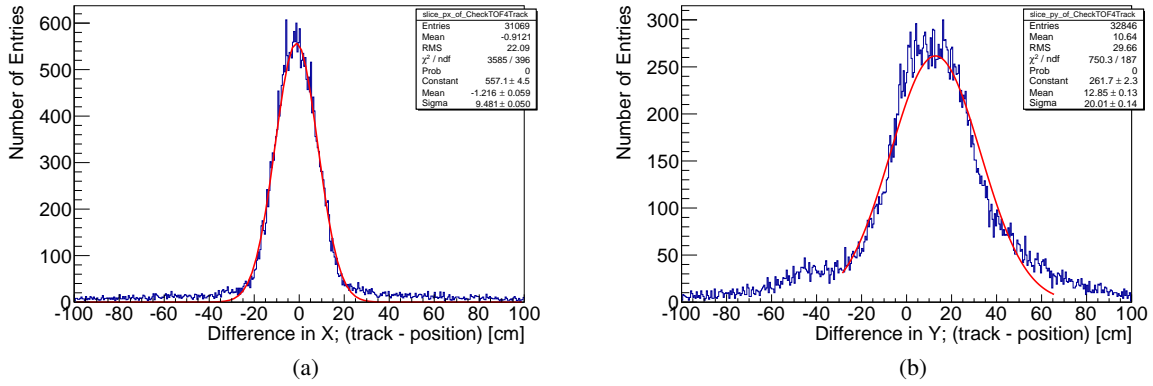
Figure 6.7: Projection and fit of data from fig. 6.5b along Y (a) and X (b) direction.
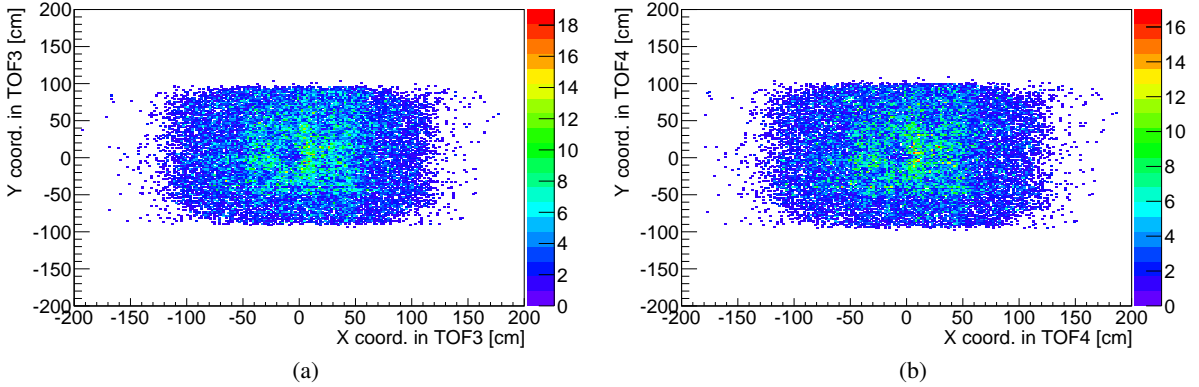
Figure 6.8: Extrapolated tracks at ToF3 (a) and ToF4 (b)

results in a significantly lower detection efficiency in the corresponding areas of ToF3 (fig. 6.10a) and ToF4 (fig. 6.10b). Both efficiency distributions show a maximum of around 40 %, while most of the detectors with a sufficient HV show values from about 15 % to 30 %.

6.3 Time of Flight Spectrum

A time of flight spectrum measured during multiple test runs based on the preliminary tracing data of [11] is shown in fig. 6.11. Using the momentum reconstruction software by [14], the time of flight of each reconstructed particle track is plotted against its momentum. Since the timing information is given relative to the trigger, negative time values can occur. The lower nearly constant branch corresponds to pions. Due to their low mass, they are emitted at $\beta \approx 1$ with almost no variation, and have a nearly constant time of flight for all momenta. The upper branch in the spectrum corresponds to protons. Due to their larger mass, they are emitted at much slower speeds than the pions ($\beta \ll 1$), and the speed therefore shows larger variations. This leads to a strong influence on their times of flight depending on the momentum. Both branches show a width of about 5 ns on the time axis, and cannot be distinguished for momenta larger than ~0.80 GeV/c. This shows that the previously mentioned extension of the ToF setup is mandatory, as the time resolutions of the individual detectors between ~400 ps and 800 ps are obviously not nearly sufficient to distinguish particles at higher incident momenta.
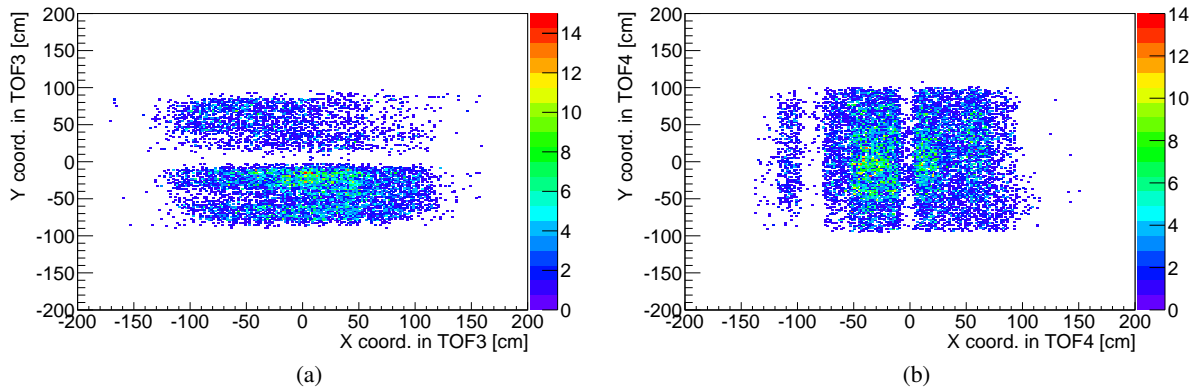
Figure 6.9: Extrapolated tracks with coincident hits at ToF3 (a) ToF4 (b)
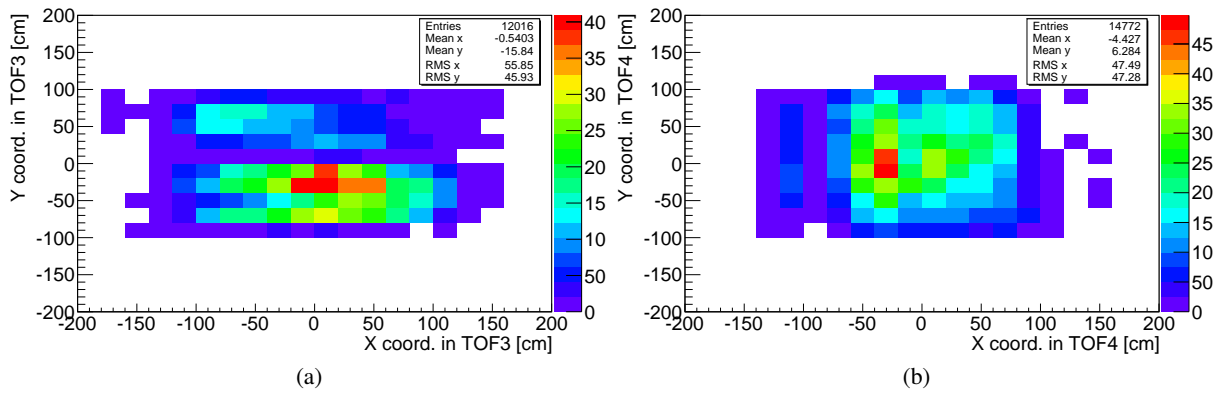
Figure 6.10: Efficiency distribution of ToF3 (a) and ToF4 (b)
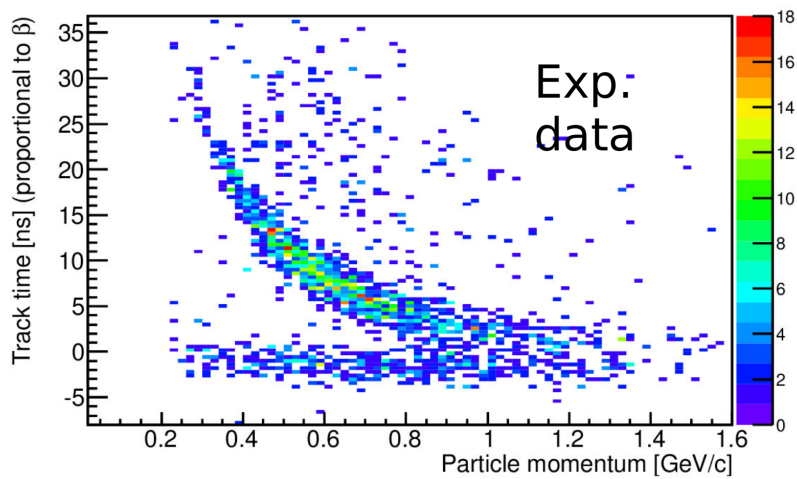
Figure 6.11: Preliminary time of flight spectrum from measured data [14].

6.4 Discussion of Results

The test of the complete ToF setup within the BGO-OD experiment have shown that the ToF spectrometer is in working condition. The SADC and the feature extraction plugin were successfully used for a first HV alignment of the detectors. The outcome of the HV alignment additionally indicates that the discarding of pileup peaks has no notable effect on the outcome. Analyzing the correlation of time difference between both ToF walls and the calculated hit position has shown that a correction of the run time differences between the TDCs of each detector is inevitable for an exact determination of the hit positions. On the other hand, the overall good correlation with extrapolated particle tracks has shown that even in the current state spatial resolutions below ~25 cm can be reached. The correlation with the extrapolated tracks additionally shows that even the preliminary tracking software provides reliable and useful results. The measured detection efficiency of only up to ~40 % is far behind the expectations given by the cosmics tests. Considering the efficiency distribution, one cause is possibly a insufficient HV value during the tests for at least some of the ToF detectors. Another cause may again come from the TDC misalignment, as the efficiency calculation only considers measured positions within a square of 20 cm around the track. The time of flight spectrum acquired with the preliminary tracking software has additionally supported the expectation that the time resolution of the ToF detectors is not sufficient for particle identification for momenta above 0.80 GeV/c.

Conclusion and Outlook

The goal of this thesis was the setup of a new time of flight spectrometer for the BGO-OD experiment using available hardware of the SAPHIR experiment based on the work of L.Schildgen. The detectors had to be characterized using cosmics, which was done by using a new cosmics test setup. All available detectors were found to be in working condition. Using the second cosmics test setup, time resolution, effective speed of light, attenuation length and detection efficiency were extracted with good precision and high statistics in a short amount of time. Therefore, the second setup has proven to be a useful and reliable option in characterization of detectors. Most of the measured values show a good agreement with the values of L.Schildgen [7].

For independent HV alignment and diagnosis of the ToF detectors, a SADC was integrated in the data readout chain of the BGO-OD experiment, and the necessary software plugins for data processing and feature extraction were developed.

Afterward, the complete ToF setup and the SADC were to be tested under real operating conditions within the BGO-OD experiment. During multiple test beam times, the SADC was successfully used for a first HV alignment of the ToF detectors, proving the usability of the current implementation of the feature extraction plugin.

First measurements of the achievable spatial resolution and detection efficiency were done by analyzing the correlation of both ToF walls, as well as the correlation of the ToF walls with extrapolated particle tracks. The measured resolutions of at least 25 cm along the detectors is in good agreement with the results from the cosmics test. The correlation between time difference of the ToF walls and the measured particle position have shown that an exact correction of offsets between the TDCs of each detector is inevitable for an exact position calculation.

This offset correction is still to be done within future test measurements, and an improvement of spatial resolution along the detectors is expected.

The efficiencies measured during the test runs showed a significant deviation from the expectations of the cosmics test, and were found to be far below the intended efficiency range above 90 %. Considering the experience gained during the cosmics test concerning the influence of insufficient HV values on efficiency, the chosen HV setting during the test runs seems to be the most probable cause.

The detection efficiency therefore has to be investigated again using a higher HV setting for all detectors in the future.

In spite of missing TDC alignment and insufficient HV settings, calculating a time of flight spectrum from measured data was still possible, showing that the ToF detector is already in a usable state.

Additionally, the time of flight spectrum shows that the extension of the ToF setup with the GRAAL - detectors is inevitable to reach a sufficient time resolution.

Complete Results of Cosmics Test

A.1 First Setup

A.1.1 Attenuation Length

Label	$Attl_\text{A}$[m]	$\Delta Attl_\text{A}$[m]	$Attl_\text{B}$[m]	$\Delta Attl_\text{B}$[m]	$Attl_\text{Avg}$[m]	$\Delta Attl_\text{Avg}$[m]
LH05 first	—	—	—	—	—	—
LH04 first	2.85	0.69	6.38	2.99	3.03	0.67
LH01 first	1.45	0.27	—	—	1.45	0.27
LH02 first	—	—	—	—	—	—
LH05 second	2.80	0.40	4.37	1.25	2.94	0.38
LH04 second	—	—	2.30	0.26	2.30	0.26
LH01 second	2.33	0.75	3.66	0.89	2.88	0.57
LH02 second	3.78	0.90	2.97	0.36	3.08	0.33
SV08	1.50	0.23	2.30	0.38	1.71	0.20
SV05	1.37	0.12	—	—	1.37	0.12
SV07	2.85	0.70	2.20	0.32	2.32	0.29
SV06	3.69	1.08	1.48	0.39	1.73	0.36

Table A.1: Attenuation lengths of first cosmics setup. Value for PM A and B of each detector, weighted mean and error propagation for average values. For the long detectors, data of both test runs is denoted accordingly. Dashed fields correspond to cases with non-converging fits. An influence due to the lower HV of the second test of the long detectors is clearly visible, as now most fits converged with useful results. SV06, SV08, LH01 and LH05 were used as reference detectors for the second Setup.

A.1.2 Effective Speed of Light

Label	Esl[m/ns]	ΔEsl[m/ns]
LH05 first	1.58×10^{-1}	2.25×10^{-3}
LH04 first	1.55×10^{-1}	2.21×10^{-3}
LH01 first	1.57×10^{-1}	2.24×10^{-3}
LH02 first	1.56×10^{-1}	2.21×10^{-3}
LH05 second	1.59×10^{-1}	4.55×10^{-3}
LH04 second	1.58×10^{-1}	4.51×10^{-3}
LH01 second	1.60×10^{-1}	4.58×10^{-3}
LH02 second	1.59×10^{-1}	4.54×10^{-3}
SV08	1.57×10^{-1}	4.30×10^{-3}
SV05	1.55×10^{-1}	4.26×10^{-3}
SV07	1.60×10^{-1}	4.34×10^{-3}
SV06	1.58×10^{-1}	4.28×10^{-3}

Table A.2: Effective speeds of light of the first cosmics setup. No influence due to changed HV within margin of error.

A.1.3 Time Resolution

Label	$TRes$[ns]	$\Delta TRes$[ns]
LH05 first	7.50×10^{-1}	1.27×10^{-2}
LH04 first	8.38×10^{-1}	1.22×10^{-2}
LH01 first	6.72×10^{-1}	1.21×10^{-2}
LH02 first	7.73×10^{-1}	1.17×10^{-2}
LH05 second	7.38×10^{-1}	1.79×10^{-2}
LH04 second	8.17×10^{-1}	1.84×10^{-2}
LH01 second	6.44×10^{-1}	1.71×10^{-2}
LH02 second	7.56×10^{-1}	1.65×10^{-2}
SV08	6.29×10^{-1}	2.35×10^{-2}
SV05	7.44×10^{-1}	2.03×10^{-2}
SV07	6.85×10^{-1}	1.76×10^{-2}
SV06	6.55×10^{-1}	1.84×10^{-2}

Table A.3: Time resolution of the first cosmics setup. No influence due to changed HV within margin of error.

A.1.4 Efficiency for MIPs

Label	$Eff[\%]$
LH05 first	99.50
LH04 first	98.40
LH01 first	97.60
LH02 first	98.40
LH05 second	98.20
LH04 second	98.10
LH01 second	97.35
LH02 second	98.20
SV08	72.28
SV05	52.42
SV07	81.37
SV06	70.08

Table A.4: Efficiencies of the first cosmics setup. Even after lowering the HV of the long detectors for the second test, no significant drop in efficiency is noticed. Due to the HV setting procedure applied for the cosmics test, the short detectors were tested with lower HVs (~1.7 kV to 1.9 kV), resulting in poor detection efficiencies.

A.2 Second Setup

A.2.1 Attenuation Length

Label	$Attl_A$[m]	$\Delta Attl_A$[m]	$Attl_B$[m]	$\Delta Attl_B$[m]	$Attl_{Avg}$[m]	$\Delta Attl_{Avg}$[m]
LH05	1.21	0.57	2.67	0.36	2.26	0.30
LH04	3.91	1.81	4.12	2.47	3.98	1.46
LH03	2.52	1.31	6.21	2.26	3.44	1.13
LH02	4.10	1.86	4.40	2.41	4.22	1.47
LH01	2.48	0.27	2.67	1.44	2.49	0.27
LH05	4.51	3.47	1.20	0.58	1.29	0.57
LH08	5.42	3.81	5.10	2.42	5.19	2.05
LH07	1.56	0.63	2.13	1.98	1.61	0.60
LH06	2.38	1.23	1.87	0.82	2.03	0.68
LH01	2.76	1.39	3.33	0.92	3.16	0.77
SV06	2.93	0.39	4.26	2.16	2.97	0.38
SV05	1.67	0.16	1.08	0.41	1.59	0.15
SV07	1.29	0.64	3.64	1.99	1.51	0.61
SV08	2.42	1.19	2.25	0.32	2.26	0.31
SV08	2.91	0.57	2.11	0.20	2.19	0.19
SV09	1.13	0.08	1.68	0.27	1.18	0.08
SV10	2.01	0.60	1.44	0.19	1.49	0.18
SV11	1.58	0.48	1.42	0.55	1.51	0.36
SV06	3.53	1.31	4.01	0.77	3.89	0.67
SV08	3.38	0.80	2.02	0.19	2.10	0.19
SV12	1.29	0.37	1.16	0.21	1.20	0.18
SV13	2.62	1.39	1.76	0.54	1.87	0.51
SV14	1.99	0.50	1.67	0.59	1.86	0.38
SV06	1.36	0.70	3.82	2.06	1.61	0.66
SV08	1.36	0.53	1.88	0.16	1.84	0.15
SV15	1.35	0.15	3.02	0.78	1.41	0.15
SV16	1.42	0.12	1.11	0.48	1.40	0.12
SV17	2.26	0.97	2.11	1.23	2.20	0.76
SV06	—	—	5.41	1.43	5.41	1.43

Table A.5: Attenuation lengths of second cosmics setup. Value for PM A and B of each detector, weighted mean and error propagation for average values. Dashed fields correspond to cases with non-converging fits. The first set of long detectors tested shows considerably larger attenuation lengths and errors, caused by the saturation effects in the ADC spectra and the limited amount of usable datapoints for each fit.

A.2.2 Effective Speed of Light

Label	Esl[m/ns]	ΔEsl[m/ns]
LH05	—	—
LH04	1.66×10^{-1}	3.83×10^{-3}
LH03	1.65×10^{-1}	3.80×10^{-3}
LH02	1.68×10^{-1}	3.87×10^{-3}
LH01	—	—
LH05	—	—
LH08	1.68×10^{-1}	3.87×10^{-3}
LH07	1.67×10^{-1}	3.86×10^{-3}
LH06	1.66×10^{-1}	3.83×10^{-3}
LH01	—	—
SV06	—	—
SV05	1.67×10^{-1}	5.07×10^{-3}
SV07	1.67×10^{-1}	5.07×10^{-3}
SV08	—	—
SV08	—	—
SV09	1.64×10^{-1}	5.00×10^{-3}
SV10	1.66×10^{-1}	5.04×10^{-3}
SV11	1.65×10^{-1}	5.02×10^{-3}
SV06	—	—
SV08	—	—
SV12	1.64×10^{-1}	4.97×10^{-3}
SV13	1.66×10^{-1}	5.04×10^{-3}
SV14	1.66×10^{-1}	5.04×10^{-3}
SV06	—	—
SV08	—	—
SV15	1.65×10^{-1}	5.02×10^{-3}
SV16	1.68×10^{-1}	5.10×10^{-3}
SV17	1.66×10^{-1}	5.05×10^{-3}
SV06	—	—

Table A.6: Effective speeds of light of second cosmics setup. Dashed fields for reference detectors. No influence of HV is noticable, however, all values are slightly higher outside the margin of error in comparison to the first setup.

A.2.3 Time Resolution

Label	$TRes$[ns]	$\Delta TRes$[ns]
LH05	6.89×10^{-1}	1.08×10^{-2}
LH04	5.88×10^{-1}	9.27×10^{-3}
LH03	6.59×10^{-1}	1.04×10^{-2}
LH02	5.47×10^{-1}	8.64×10^{-3}
LH01	7.03×10^{-1}	1.11×10^{-2}
LH05	6.85×10^{-1}	1.16×10^{-2}
LH08	6.00×10^{-1}	1.08×10^{-2}
LH07	6.03×10^{-1}	1.09×10^{-2}
LH06	7.18×10^{-1}	1.24×10^{-2}
LH01	7.22×10^{-1}	1.24×10^{-2}
SV06	6.74×10^{-1}	1.06×10^{-2}
SV05	5.37×10^{-1}	8.58×10^{-3}
SV07	4.24×10^{-1}	6.88×10^{-3}
SV08	5.29×10^{-1}	8.40×10^{-3}
SV08	7.17×10^{-1}	1.15×10^{-2}
SV09	5.87×10^{-1}	9.65×10^{-3}
SV10	5.39×10^{-1}	9.05×10^{-3}
SV11	5.00×10^{-1}	8.24×10^{-3}
SV06	5.34×10^{-1}	8.70×10^{-3}
SV08	7.02×10^{-1}	1.13×10^{-2}
SV12	5.68×10^{-1}	9.53×10^{-3}
SV13	5.39×10^{-1}	9.14×10^{-3}
SV14	4.95×10^{-1}	8.08×10^{-3}
SV06	5.29×10^{-1}	8.55×10^{-3}
SV08	6.74×10^{-1}	1.07×10^{-2}
SV15	5.03×10^{-1}	8.07×10^{-3}
SV16	4.67×10^{-1}	7.52×10^{-3}
SV17	4.36×10^{-1}	7.01×10^{-3}
SV06	5.13×10^{-1}	8.15×10^{-3}

Table A.7: Time resolutions of second cosmics setup.

A.2.4 Efficiency for MIPs

Label	$Eff[\%]$
LH05	—
LH04	97.14
LH03	89.65
LH02	97.11
LH01	—
LH05	—
LH08	98.79
LH07	96.76
LH06	97.60
LH01	—
SV06	—
SV05	58.39
SV07	90.79
SV08	—
SV08	—
SV09	57.28
SV10	71.03
SV11	52.02
SV06	—
SV08	—
SV12	42.96
SV13	80.53
SV14	73.15
SV06	—
SV08	—
SV15	83.28
SV16	57.89
SV17	79.49
SV06	—

Table A.8: Efficiencies of second cosmics setup. Dashed fileds indicate the reference detectors. The strong deviations in detection efficiencies between short and long detecotrs is found to be a purely HV related effect.

Bibliography

[1] O. Jahn, personal communication, 2013.

[2] D. Baur, "Das Szintillationszählersystem am SAPHIR Detektor", 1989.

[3] Particle Data Group, "Passage of Particles Through Matter" (2012), URL:
     http://pdg.lbl.gov/2012/reviews/rpp2012-rev-passage-particles-matter.pdf.

[4] W. R. Leo, *Techniques for nuclear and particle physics experiments: a how-to approach*,
     Springer, 1994.

[5] H. Kolanoski, Lecture Script, 2007,
     URL: http://www-zeuthen.desy.de/~kolanosk/det07/skripte/wwmat01.pdf.

[6] G. Knoll, *Radiation detection and measurement*, Wiley, 1989, ISBN: 9780471815044,
     URL: http://books.google.de/books?id=dyBRAAAAMAAJ.

[7] L. Schildgen, "Charakterisierung des Antwortverhaltens der Time-of-Flight-Detektoren des
     BGO-OD Experiments", Bachelor Thesis, 2012.

[8] J. Hanappel, personal communication, 2013.

[9] R. Giles, F. Pipkin and J. Wolinski, "Tests of conventional and microchannel plate
     photomultipliers as components of a scintillation time-of-flight system",
     *Nuclear Instruments and Methods in Physics Research Section A: Accelerators, Spectrometers,
     Detectors and Associated Equipment* 252.1 (1986) 41–52.

[10] A. Ramseger,
      "Vorbereitung und Test des Flugzeitdetektors für das Crystal-Barrel-Experiment an ELSA".

[11] T Jude and V Vegna, Track reconstruction plugins for ROOT EXPLORA, 2013.

[12] T. Jude, Simulation of particle momentum, 2013.

[13] *Technical Information Manual Revision n.6, for CAEN MOD.V1742 32+2 Ch 12 Bit 5GS/s
      Digitizer*.

[14] T. Jude, Momentum recostruction software for ROOT EXPLORA, 2013.

List of Figures

64

List of Tables

Danksagung / Acknowledgements